CONTROL OF FLOW STRUCTURE ON 70° SWEPT DELTA WING WITH ALONG-THE-CORE BLOWING USING NUMERICAL MODELING

A THESIS SUBMITTED TO
THE GRADUATE SCHOOL OF NATURAL AND APPLIED SCIENCES
OF
MIDDLE EAST TECHNICAL UNIVERSITY

BY

İBRAHİM CAN KÜÇÜKYILMAZ

IN PARTIAL FULFILLMENT OF THE REQUIREMENTS
FOR
THE DEGREE OF MASTER OF SCIENCE
IN
MECHANICAL ENGINEERING

JANUARY 2016

Approval of the thesis:

CONTROL OF FLOW STRUCTURE ON 70° SWEPT DELTA WING WITH ALONG-THE-CORE BLOWING USING NUMERICAL MODELING

submitted by **İBRAHİM CAN KÜÇÜKYILMAZ** in partial fulfillment of the requirements for the degree of **Master of Science in Mechanical Engineering Department, Middle East Technical University** by,

Prof. Dr. Gülbin Dural Ünver _____
Dean, Graduate School of **Natural and Applied Sciences**

Prof. Dr. Tuna Balkan _____
Head of Department, **Mechanical Engineering**

Assoc. Prof. Dr. M. Metin Yavuz _____
Supervisor, **Mechanical Engineering Dept., METU**

Examining Committee Members:

Prof. Dr. Kahraman Albayrak _____
Mechanical Engineering Dept., METU

Assoc. Prof. Dr. M. Metin Yavuz _____
Mechanical Engineering Dept., METU

Assoc. Prof. Dr. Yiğit Yazıcıoğlu _____
Mechanical Engineering Dept., METU

Asst. Prof. Dr. Cüneyt Sert _____
Mechanical Engineering Dept., METU

Assoc. Prof. Dr. Selin Aradağ _____
Mechanical Engineering Dept., TOBB ETU

Date: 21/01/2016

I hereby declare that all information in this document has been obtained and presented in accordance with academic rules and ethical conduct. I also declare that, as required by these rules and conduct, I have fully cited and referenced all material and results that are not original to this work.

Name, Last name : İbrahim Can KÜÇÜKYILMAZ

Signature :

ABSTRACT

CONTROL OF FLOW STRUCTURE ON 70° SWEPT DELTA WING WITH ALONG-THE-CORE BLOWING USING NUMERICAL MODELING

Küçükyılmaz, İbrahim Can
M.S., Department of Mechanical Engineering
Supervisor: Assoc. Prof. Dr. Mehmet Metin Yavuz

January 2016, 93 pages

In recent years, interest has increased in Unmanned Combat Air Vehicles (UCAVs) and Unmanned Air Vehicles (UAVs), which can be represented by simplified planforms including delta wings. Delta wings experience the formation of two counter-rotating vortices on the leeward side of the planform due to the shear layer separated from the windward side. At sufficiently high angle of attack, these vortices undergo sudden expansion, called vortex breakdown/burst, which is quite detrimental considering the aerodynamic performance of the wing. The present study investigates the Computational Fluid Dynamics (CFD) simulations of these vortical structures and the associated flow control with along-the-core blowing around 70° swept delta wing to primarily delay breakdown/burst location of these vortical structures.

In the present study, different turbulence models with varied corrections are investigated using the commercially available software in order to predict the formation and breakdown of vortical structures accurately. Firstly, a mesh independency study is successfully achieved, and then detailed validation of the CFD models is carried out using previously conducted experimental studies. k-ω

SST with curvature correction turbulence model is selected as the best numerical approach considering the accuracy of the results. In addition, along-the-core blowing control technique is applied to delay the vortex breakdown location. The effects of momentum coefficient and pitch angle on vortex breakdown location are investigated in detail. Pitch angles ranging from 7.5° to 60° are examined, and the results indicate that maximum vortex breakdown delay is achieved at pitch angles from 7.5° to 30°. Further increase in pitch angle decreases the effect of core blowing on flow structure and leads to less delay in vortex breakdown location. The results also indicate that as momentum coefficient increases, vortex breakdown delay increases almost linearly with the defined momentum coefficient interval ranging from 0.008 to 0.048.

Keywords: Delta wing, Leading edge vortex, Vortex breakdown, CFD, Along-the-core blowing

ÖZ

70° SÜPÜRME AÇISINA SAHİP DELTA KANAT ÜZERİNDEKİ AKIŞ YAPISININ GİRDAP MERKEZİ BOYUNCA ÜFLEME İLE KONTROLÜNÜN NUMERİK ÇÖZÜMÜ

Küçükyılmaz, İbrahim Can
Yüksek Lisans, Makina Mühendisliği Bölümü
Tez Yöneticisi: Doç. Dr. Mehmet Metin Yavuz

Ocak 2016, 93 sayfa

Basitleştirilmiş platformlarla temsil edilebilen insansız savaş araçları ve insansız hava araçlarına (delta kanatlar da dahil olmak üzere) son yıllarda artan bir ilgi vardır. Delta kanadın rüzgar alan tarafından sınır tabakasının ayrılması neticesinde, delta kanadın üst yüzeyinde tersine dönen iki girdap oluşumu tecrübe edilmektedir. Yeterli yükseklikteki hücum açısında, söz konusu girdaplar ani genişlemeye maruz kalmakta (bu durum, girdap çökmesi/girdap patlaması olarak da isimlendirilmekte) ve kanadın aerodinamik performansına zarar vermektedir. Mevcut çalışma, hesaplamalı akışkanlar dinamiği (HAD) ile 70° süpürme açısına sahip delta kanat üzerindeki girdaplı yapıların modellenmesini ve girdap merkezi boyunca üfleme akış kontrolüyle, öncelikli olarak girdapların çökme yerlerinin ertelenmesini incelemektedir.

Mevcut çalışmada ticari yazılım kullanılarak; girdaplı yapıların oluşması ve çökmesini isabetli olarak tahmin edebilmek amacıyla farklı türbülans modelleriyle birlikte çeşitli düzeltmeler incelenmiştir. İlk olarak sayısal ağdan bağımsızlık çalışması başarılı bir şekilde gerçekleştirilmiş ve önceki deneysel veriler

kullanılarak, HAD modellerinin doğrulaması yapılmıştır. “k-ω SST - curvature correction” türbülans modeli, sonuçların hassasiyeti göz önüne alındığında en iyi numerik yaklaşım seçilmiştir. Buna ek olarak, girdap merkezi boyunca üfleme kontrol yöntemi girdap çökme konumunun ertelenmesi amacıyla uygulanmıştır. Momentum katsayısının ve yunuslama açısının girdap çökme konumuna etkisi ayrıntılı şekilde incelenmiştir. 7.5° ile 60° arasındaki yunuslama açısı incelenmiştir ve sonuçlar; yunuslama açısının 7.5°’den 30°’ye kadar olduğu aralıkta maksimum girdap çökme konumu ertelemesinin gerçekleştiğini göstermiştir. Yunuslama açısındaki ilave artış girdap merkezi boyunca üflemenin akış yapısındaki etkisini azaltmakta ve girdap çökme konumunun daha az ertelenmesine yol açmaktadır. 0.008’den 0.048’e kadar tanımlanan momentum katsayı aralığında; momentum katsayısının artmasıyla, girdap çökmesinin ertelenmesinin neredeyse doğrusal olarak artmakta olduğunu sonuçlar göstermektedir.

Anahtar Kelimeler: Delta kanat, Kanat ucu girdabı, Girdap çökmesi, Hesaplamalı Akışkanlar Dinamiği, Girdap merkezi boyunca üfleme

To My Parents …

ACKNOWLEDGEMENTS

I would like to express my deepest gratitude to my supervisor Assoc. Prof. Dr. M. Metin Yavuz, for his guidance, advice, criticism, encouragements and insight throughout the research.

I would like to thank my colleagues Latif Kesemen, Uğur Koç, Çağlayan Durlu and Tuğberk İncekürk for their support and guidance.

I would like to thank Yiğit Yücel, Onur Özkan, Berkan Çifçi, İlkan Yıldırım and especially Selda Gürsoy for their endless support and precious friendship. Without them it would be impossible for me to finish this study.

Last but not the least; I would like to thank my beloved immediate family: my parents Bilge Küçükyılmaz and Rıza Küçükyılmaz and my grandmother Zekiye Şimşek for their continuous support, tolerance and trust throughout my life.

TABLE OF CONTENTS

ABSTRACT v

ÖZ vii

ACKNOWLEDGEMENTS x

TABLE OF CONTENTS xi

LIST OF TABLES xiii

LIST OF FIGURES xiv

LIST OF SYMBOLS xviii

CHAPTERS

1. INTRODUCTION 1

1.1 Motivation of the Study 2

1.2 Aim of the Study 3

2. LITERATURE REVIEW 5

2.1 Flow Features of Leading Edge Vortices 5

2.1.1 Leading edge vortices 5

2.1.2 Vortex breakdown 6

2.1.3 Aerodynamic characteristics 7

2.1.4 Shear layer instability 8

2.1.5 Vortex wandering 9

2.1.6 Helical mode instability 10

2.1.7 Oscillations of breakdown location 10

2.1.8 Vortex shedding 11

2.2 Previous Studies on 70° Delta Wing Studied in the Thesis 11

2.2.1 Experimental studies 12

2.2.2 Numerical studies 16

2.3 Vortex Breakdown Flow Control Mechanisms on Delta Wings 21

2.3.1 Mechanical devices 23

2.3.2 Pneumatic techniques 24

2.3.2.1 Along the core blowing 26

2.3.2.1.1 Along the core blowing on 70° swept delta wing studied in this thesis 28

2.3.3 Numerical studies on the control of leading edge vortices 29

3. SIMULATION MODEL 45

3.1 Simulation Domain, Boundary Conditions, and Simulation Parameters 45

3.2 Grid Information, Mesh Independence and Computation Time 46

4. COMPARISON AND VERIFICATION OF TURBULENCE MODELS 55

5. FLOW CONTROL 67

6. CONCLUSIONS 73

6.1 Summary and Conclusions 73

6.2 Future Work 75

REFERENCES 77

APPENDICES 85

A. TURBULENCE MODELING 85

A1. Reynolds Averaging and Boussinesq Approach 85

A2. Shear-Stress Transport (SST) k-ω Model 87

LIST OF TABLES

TABLES

Table 3.1 Dimensions of the simulation domain in terms of root chord 49
Table 3.2 Details of the boundary conditions..... 49
Table 3.3 Details of grids used in mesh independency study 49
Table 3.4 Vortex breakdown locations of four cases..... 52
Table 3.5 The computation time of four mesh cases 54
Table 4.1 Vortex breakdown location of turbulence models 58
Table 4.2 Vortex breakdown location of previous numerical studies 62
Table 4.3 Suction peak at three different chordwise locations..... 62
Table 4.4 Angle between the vortex core and the leeward surface at three different chordwise locations..... 62
Table 4.5 Vortex sweep angle at three different chordwise locations 63
Table 5.1 First set of simulations..... 70
Table 5.2 Second set of simulations 71

LIST OF FIGURES

FIGURES

Figure 1.1 Interaction of burst strake vortex with twin tail of NASA's F-18 High Angle of Attack Research Vehicle (HARV) [3] 4
Figure 1.2 Interaction between forebody and burst strake vortices [3] 4
Figure 2.1 Schematic of the flow field over the leeward surface of delta wing at angle of attack [3] 31
Figure 2.2 Velocity distribution in the vortex core before breakdown [4] 31
Figure 2.3 Spiral and bubble type vortex breakdown [7] 32
Figure 2.4 Sense of azimuthal vorticity [12] 32
Figure 2.5 Lift coefficients for flat plate delta wings having sweep angle between a) 60° - 70°, b) 70° - 85° [4] 33
Figure 2.6 Dimensionless frequency variation for unsteady phenomena as a function of AoA [13] 34
Figure 2.7 The non-dimensional frequency range of unsteady flow phenomena over delta wings [13] 34
Figure 2.8 Delta wing configuration: a) schematic, b) real model in the experiment [20, 21] 35
Figure 2.9 Experimental configuration of delta wing in F2 tunnel [21] 35
Figure 2.10 Instant images of laser sheet: a) side view, b) close view to vortex breakdown location [21] 36
Figure 2.11 Evolution of breakdown location as a function of AoA [21] 36
Figure 2.12 Surface oil flow visualization at AoA = 27° and U_∞ = 24 m/s [21] 37
Figure 2.13 Cp contour on the upper surface of the delta wing at AoA = 27° and freestream velocity of 24 m/s [21] 37
Figure 2.14 Non-dimensional axial velocity at AoA = 27° and U = 24 m/s at four different planes perpendicular to upper surface: X = 500 mm, X = 600 mm, X = 700 mm, X = 800 mm [21] 38

Figure 2.15 Non-dimensional axial vorticity at AoA = 27° and U = 24 m/s at four planes perpendicular to upper surface: X = 500 mm, X = 600 mm, X = 700 mm, X = 800 mm [21] 38
Figure 2.16 Non-dimensional turbulent kinetic energy at AoA = 27° and U = 24 m/s at four planes perpendicular to upper surface: X = 500 mm, X = 600 mm, X = 700 mm, X = 800 mm [21] 39
Figure 2.17 Non-dimensional axial velocity contour in the plane which longitudinally intersects vortex core at AoA = 27° and U = 24 m/s [21] 39
Figure 2.18 Non-dimensional TKE contour in the plane which longitudinally intersects vortex core at AoA = 27° and U = 24 m/s [21] 40
Figure 2.19 LDC results of non-dimensional axial vorticity at 14 different planes perpendicular to the leeward surface of the delta wing [15] 40
Figure 2.20 Effects of various flow control methods on leading edge vortices of a 60^0 sweep slender delta wing with sharp leading edges at an angle of attack of 20^0: a) Obstacle located downstream, b) Trailing edge suction, c) Flow ejection counter to the axial velocity of the vortex core, and d) Along-the-core blowing to left side of vortex [32] 41
Figure 2.21 Flaps located at leading edge and variable sweep equipment studied by Gursul et al. [32] 42
Figure 2.22 Location of five blowing nozzles for along the core blowing [34] 42
Figure 2.23 Performance of blowing as a function of azimuthal angle with constant blowing coefficient (C_μ = 0.01) [34] 43
Figure 2.24 Relationship between breakdown location and blowing momentum for three azimuthal angles [34] 43
Figure 2.25 Effectiveness of blowing/suction control techniques [47] 44
Figure 2.26 Effectiveness comparison of steady and unsteady blowing [47] 44
Figure 3.1 Simulation domain 48
Figure 3.2 Mesh 3: a) General view, and b) Sectional view 50
Figure 3.3 Convergence history of the simulation 51
Figure 3.4 Four chordwise line stations (X = 500 mm, X = 600 mm, X = 700 mm, and X = 800 mm) 51

Figure 3.5 Pressure coefficient (Cp) – iteration chart of Mesh 3 52
Figure 3.6 Azimuthal vorticity contour of a) Mesh 1, b) Mesh 2, c) Mesh 3, and d) Mesh 4 53
Figure 3.7 Pressure coefficients of four cases at four different chordwise locations: a) X = 500 mm, b) X = 600 mm, c) X = 700 mm, and d) X = 800 mm 54
Figure 3.1 Simulation domain 48
Figure 3.2 Mesh 3: a) General view, and b) Sectional view 50
Figure 3.3 Convergence history of the simulation 51
Figure 3.4 Four chordwise line stations (X = 500 mm, X = 600 mm, X = 700 mm, and X = 800 mm) 51
Figure 3.5 Pressure coefficient (Cp) – iteration chart of Mesh 3 52
Figure 3.6 Azimuthal vorticity contour of a) Mesh 1, b) Mesh 2, c) Mesh 3, and d) Mesh 4 53
Figure 3.7 Pressure coefficients of four cases at four different chordwise locations: a) X = 500 mm, b) X = 600 mm, c) X = 700 mm, and d) X = 800 mm 54
Figure 4.1 Azimuthal vorticity contour passing through vortex core: a) k-ω LRC SFC CC, b) k-ω SST, c) k-ω SST LRC, d) k-ω SST CC, e) k-ω SST LRC CC, f) SA, and g) SA CC 59
Figure 4.2 Pressure coefficients of four cases at four different chordwise locations: a) X = 500 mm, b) X = 600 mm, c) X = 700 mm, and d) X = 800 mm 60
Figure 4.3 Pressure coefficient comparison of previous numerical studies at four different chordwise locations: a) X = 500 mm, b) X = 600 mm, c) X = 700 mm, and d) X = 800 mm 61
Figure 4.4 Computed (left) and measured [21] (right) pressure distribution of the leeward surface 63
Figure 4.5 Computed (left) and measured [21] (right) non-dimensional axial velocity (U / U_0) at four planes perpendicular to the leeward surface of the delta wing: a) X = 500 mm, b) X = 600 mm, c) X = 700 mm, and d) X = 800 mm 64
Figure 4.6 Computed (left) and measured [21] (right) non-dimensional axial vorticity ($\Omega_x c / U_0$) at four planes perpendicular to leeward surface of the delta wing: a) X = 500 mm, b) X = 600 mm, c) X = 700 mm, and d) X = 800 mm 65

Figure 4.7 Computed (left) and measured [21] (right) non-dimensional turbulent kinetic energy ($k / (U_0)^2$) at four planes perpendicular to the leeward surface of the delta wing: a) X = 500 mm, b) X = 600 mm, c) X = 700 mm, and d) X = 800 mm 66
Figure 5.1 Location of the blowing port 69
Figure 5.2 Jet blowing angle: a) Azimuthal angle, b) Pitch angle [45] 70
Figure 5.3 Results of the first set of simulations 70
Figure 5.4 Results of the second set of simulations..... 71
Figure 5.5 Non-dimensional axial velocity contour at a plane passing through the vortex core for a) non-controlled case, and b) controlled case, m1..... 72

LIST OF SYMBOLS

A1	Primary attachment line
c	Root chord (RC)
Cμ	Momentum coefficient
Cp	Pressure coefficient
e	Semi-span
k	Turbulent kinetic energy (m^2/s^2)
$\dot{m}$	Mass flow rate of jet (kg/s)
μ_t	Turbulent viscosity (Pa.s)
q_0	Dynamic pressure (Pa)
Re	Reynolds number
S	Wing planform area (m^2)
S1	Primary separation line
S2	Secondary separation line
U	Axial velocity (m/s)
U_0	Freestream velocity (m/s)
V_j	Jet exit velocity (m/s)
Y	Cartesian coordinate – y direction
X_b	Vortex breakdown location

ΔC_N	Change in normal force coefficient
ΔX_{bd}	Change in breakdown location
γ	Helix angle (°)
y^+	A non-dimensional wall distance
Ω_x	Axial vorticity (1/s)
Λ	Sweep angle (°)
ε	Turbulence dissipation rate (m^2/s^3)
ω	Specific turbulence dissipation rate (1/s)
AoA	Angle of attack
CC	Curvature correction
CFD	Computational fluid dynamics
DES	Detached eddy simulation
LDV	Laser doppler velocimetry
LRC	Low Reynolds correction
PIV	Particle image velocimetry
RSM	Reynolds stress model
SA	Spalart Allmaras
SARC	Spalart Allmaras rotation correction
SST	Shear stress transport
TKE	Non-dimensional turbulent kinetic energy

CHAPTER 1

INTRODUCTION

The trend of current aircraft design is progressing to reduce the angle of attack limitations in low-speed flight. High swept delta wings with sharp leading edge and variations on these kinds of delta wings are commonly seen among high-performance aircraft [1].

Preventing flow separation was one of the early major design considerations. However, the increase in aircraft speed as well as the need for avoiding compressibility effects has led to increasing the sweep angle of delta wings and decreasing the thickness of the wings. However; with this configuration, difficulties were experienced in preventing flow separation so that delta wing flow characteristics began to be studied in detail. These swept wings offer good high angle of attack (AoA) characteristics at low speed and low drag characteristics at high speed [1].

With sufficient sweep, delta wings can continue producing lift up to an angle of attack of 40°. Complete separation of flow from the wing upper surface that causes loss of lift (stall) is faced at much lower angles of attack for finite wings with high aspect ratio. On the other hand, flow separates at the primary separation line of the delta wing (leading edge) at around AoA of 5° and then these separated layers form stationary vortices. These vortices provide suction near the leading edge and contribute to lift. In other words, vortical structures that are the results of flow separation contribute to lift gain [1-2].

The strength of these vortical structures increases with AoA until the occurrence of sudden disorganization, known as vortex breakdown or vortex burst. This phenomenon causes rapid changes in the forces and moment exerted on aircraft

and leads to unexpected aerodynamic instability. The interaction of the burst strake vortex with the twin tail of NASA's F-18 High Angle of Attack Research Vehicle (HARV) is shown in Figure 1.1. These interactions are known to cause tail buffet, which can lead to structural fatigue of the aft control surfaces or the entire tail assembly. Figure 1.2 shows the interaction between forebody and burst strake vortices over the same aircraft. This vortex interaction can cause wing rock phenomena [3].

Computational Fluid Dynamics (CFD) is a powerful tool for producing numerical solutions to a system of partial differential equations that describes the fluid flow. CFD helps engineers to understand the entire flow field qualitatively and quantitatively so that CFD is often used to improve engineering design [3]. In addition, simulation conditions as well as simulation models could be easily changed to determine their effect. More realistic flight conditions can be simulated via CFD tools when compared with wind tunnel experiments. Wall effects, influence of structures which hold the test item in the tunnel, and the extreme conditions for wind tunnel testing (hypersonic aircraft flight) are the main disadvantages of wind tunnels. On the other hand, the challenges of understanding turbulence guarantee the wind tunnel a continued use. To achieve successful design, the intelligent combination of both methods should be utilized [1].

1.1 Motivation of the Study

Delta wings are used for fighter aircraft, micro air vehicles, and unmanned combat air vehicles for their high maneuverability and additional lift gain by vortical structures. At sufficiently high angles of attack, breakdown of these vortical structures occur and this phenomenon causes loss of lift, loss of stability, and large amplitude unsteady loading, leading to structural damage of the wing. Because of the undesired effects of the breakdown mechanism, there are many active and passive vortex control techniques to delay or eliminate vortex breakdown. CFD

modeling of highly complex flow around delta wings and predicting the vortex breakdown location are important to increase the level of understanding and to investigate the effect of various control mechanisms. Therefore, CFD models will be utilized to model the complex flow structure around delta wings, and along-the-core blowing technique will be used to delay the vortex breakdown location in this study.

1.2 Aim of the Study

In the current study, flow over the delta wing having 70° sweep angle is investigated in detail using steady Reynolds-Averaged Navier-Stokes (RANS)-based turbulence modeling. The aim of the study is firstly to compare the mesh-independent CFD results having different turbulence models with varied corrections and to validate the model against experimental data. Vortex breakdown location, surface pressure, non-dimensional axial velocity contour, non-dimensional axial vorticity contour, and non-dimensional turbulent kinetic energy contour at a plane perpendicular to the upper side of the delta wing are the calculations used for turbulence model comparison and validation. After the validation, applying along-the-core blowing control technique by altering the two parameters (Cμ and pitch angle) and witnessing the improvement in the flow field are described.

Figure 1.1 Interaction of burst strake vortex with twin tail of NASA's F-18 High Angle of Attack Research Vehicle (HARV) [3]

Figure 1.2 Interaction between forebody and burst strake vortices [3]

CHAPTER 2

LITERATURE REVIEW

In this chapter; literature review of leading edge vortices, vortex breakdown phenomenon on delta wings, aerodynamic characteristics of delta wings and instabilities of flow over delta wing including shear layer instability, vortex wandering, helical mode instability, oscillation of vortex breakdown and vortex shedding are investigated in detail.

2.1 Flow Features of Leading Edge Vortices

2.1.1 Leading edge vortices

Figure 2.1 shows the simplified flow structure above a delta wing [3]. The roll up of shear layer or vortex sheet generates the counter-rotating leading edge vortices. These curved free shear layers are formed by separation of flow at the leading edge so called primary separation line labeled as S_1 and reattaches along the primary attachment line A_1 in Figure 2.1. Leading edge vortices promote the entrained flow to move in spanwise directions. This outward flow can be separated from leeward surface of the delta wing at secondary separation line denoted as S_2 due to adverse pressure gradients and can form a secondary vortices having opposite sign with respect to primary vortices. Following the same process, even tertiary vortices can be formed.

Leading edge vortex can be characterized as ‘swirling jet flows’. Swirling jet flows description is illustrated at Figure 2.2 which shows the velocity distribution through the primary vortex as a function of AoA [4]. It is clearly seen that as the

AoA increases, magnitude of both axial and tangential velocity at vortex core increase. Jet velocity at vortex core can reach up to three or more times the freestream velocity depending upon sweep angle of delta wing [4].

Primary vortex core moves inboard and upwards above the surface of the delta wing as a result of formation of secondary vortices [1]. According to Visbal's [5] work, position and size of secondary vortex depend not only on AoA and sweep angle but also on Reynolds number. Leading edge vortex sweep angle is almost independent of range of interest in AoA and approximately proportional to the sweep angle of the delta wing. The angle between leeward surface and vortex core increases linearly with AoA. Size of leading edge vortex core also has Reynolds number independence. Vortex core grows linearly in direction of downstream forming conical shape [5].

2.1.2 Vortex breakdown

Counter-rotating leading edge vortices cannot maintain their stability over the delta wing at all AoA. At sufficiently high AoA, jet like velocity in the core of the vortex stagnates and experiences a rapid enlargement also known as vortex breakdown. This phenomenon was first described by Werle (1954) [6].

Lambourne et al. [7] introduced two distinct type of vortex breakdown which are spiral and bubble type breakdown. Detailed view of these two type breakdown is given at Figure 2.3. Lopez and Brown et al. [8, 9 and 12] showed that negative azimuthal vorticity slows down the axial velocity and eventually lead to stagnation and recirculation. Sense of azimuthal vorticity is given at Figure 2.4. Previous work of Delery and Benjamin [10, 11, 12] showed that change in criticality of the vortical flow that is determined by maximum helix angle (defined as ratio of arctangent of azimuthal velocity to axial velocity [12]) can be linked to onset of vortex breakdown.

Very early studies of Lambourne et al. [1, 7] mentioned some factors affecting the breakdown position. Some of them are given below:

- As AoA is increased, vortex breakdown position moves to upstream.
- As the aspect ratio increases, breakdown moves upstream (vice versa) for the delta wings having sweep angle less than 75°.
- Acceleration of free stream flow changes the position of the vortex breakdown. Increase in velocity, moves the breakdown location to upstream because upstream of the wing has initially higher velocity with lower pressure compared to downstream region of the wing. With the help of this adverse pressure gradient, breakdown location move upwards until the all flow field reach new velocity. After reaching new velocity, breakdown returns to its original position.
- Effect of Reynolds number (Re) in the range of $1\times10^4 \leq Re \leq 4.6\times10^6$ were found to be small on vortex breakdown location for delta wings with sharp leading edges.

According to both experiments and theoretical explanations reviewed by Gursul [13], swirl level and external pressure gradient outside the vortex core are two important parameters affecting the occurrence and movement of vortex breakdown. Earlier occurrence of breakdown is promoted by increase in either of these two parameters. Gursul also stated that both parameters depend on AoA and sweep angle.

2.1.3 Aerodynamic characteristics

Leading edge vortices over delta wing accelerate the flow locally. This local acceleration of flow creates a local suction peak on the leeward surface of the wing beneath the primary vortices. In addition to potential lift, local suction peak provides significant lift, also known as vortex lift. Character of vortex-induced lift is nonlinear with respect to AoA.

Lift coefficient is on the order of 1.0 to 1.4 for high sweep delta wings and lift coefficient mainly depends on sweep angle. Leading edge vortices produce between 30% and 60% of the total lift at high AoA [3].

Figure 2.5 shows the effect of vortex breakdown on the lift characteristics of delta wings with different sweep angles [4]. Vortex breakdown occurs over the wing (up to the trailing edge) fairly early before the maximum lift occurs for low sweep delta wings. On the other hand, AoA at which vortex breakdown crosses the trailing edge approaches the AoA for the maximum lift in case of delta wings with higher sweep angles. These two AoA values are almost equal for the delta wings having sweep angles equal or greater than 75^0.

To sum up, adverse effects on time average performance of delta wing like decrease of lift and pitching moment are due to vortex breakdown phenomenon [13]. In addition, vortex breakdown is the one of the most important well known source of buffeting of slender delta wings [14]. There are numbers of unsteady characteristics of flow over slender delta wings affecting stability, control and wing/fin buffeting. These unsteady phenomena will also be discussed in this chapter.

2.1.4 Shear layer instability

Vortical substructures placed in the separated shear layers have been observed by many researchers who came to conclusion with two contrast descriptions: substructures rotating around the leading edge vortex (temporal) and spatially fixed substructures around the periphery of the leading edge vortex [15]. It is confirmed that both type substructures are not definitely two separate incidents [13, 16].

Researchers also came with ideas about type of instability causing the formation of the vortical substructures but none of them has been accepted or proven. The most popular of the proposed hypotheses is that substructures form in a similar manner to the Kelvin-Helmholtz instability or instability of the shear layer (two

dimensional) expressed by Ho et al. [15]. According to another idea, interaction between the separating shear layer and secondary vortices induces the transversal perturbations along the leading edge. Hence, these substructures originate from these perturbations. Wasburn et al. [15] suggested that flow in the transverse direction at the leading edge vortices originates non-viscous instabilities in the detached layer and these non-viscous instabilities generate these substructures. Hypothesis like axial instability related with curvature of the detached shear layer, existence of surface waves in low amplitude in the water tunnel and vibrations in a wind tunnel were suggested as a cause of forming of these substructures. These entire suggested hypotheses have not been universally accepted or proved [15].

2.1.5 Vortex wandering

Random displacement of vortex core is called as vortex wandering [17]. Menke et al. [18] encountered velocity fluctuations in large amplitude even in the nonappearance of vortex breakdown over delta wing. Kommallein et al. [13] and Schmucker et al. [13] concurrently noticed the considerable fluctuations in the velocity of the vortex core on the leeward side of the delta wings. Cornelius [13] had the same observation over an aircraft model and Degani et al. [13] encountered velocity fluctuations over an ogive cylinder. Irrespective of Reynolds number and geometry, high amplitude fluctuations in velocity were observed in the core of the vortex due to vortex wandering [13].

Baker et al. [13] and Devenport et al. [13] suggested that vortex wandering in the tip vortices originate from freestream turbulence. However, Menke and Gursul [18] pointed out that displacement of vortex core is much larger than caused by freestream turbulence for leading edge vortices. Unsteady wake turbulence of the wing, K-H instability and nonlinear interactions of small vortices and primary vortex were also discussed to be the potential source of vortex wandering over delta wings [13].

2.1.6 Helical mode instability

Helical mode instability, which is a hydrodynamic instability, exists after the breakdown. In the downstream of breakdown for various type swirling flows, oscillations were observed periodically. Sufficient information is available on the relationship between dominant frequency of helical mode instability and the wing geometry including AoA and angle of sweep. This information is useful for buffeting complications, especially fin buffeting [13].

2.1.7 Oscillations of breakdown location

Experiments of Lowson [13] showed that breakdown location of vortices over still delta wing is unsteady and displays fluctuations along the vortical axis. It was also revealed by Ayoub et al.'s [13] study that breakdown location oscillations of left and right vortices are anti-symmetric. Gursul [13] stated breakdown oscillations could be substantial for the stability of the aircraft which is highly maneuverable and breakdown oscillations may lead significant outcomes for the buffeting of wing and tail.

When the time averaged breakdown locations of counter-rotating vortices get closer to each other, more coherent and larger oscillations were detected. Breakdown locations get closer when either AoA or angle of sweep is augmented. These vortex interactions generally related to slender delta wings, but such interactions with sweep angle of 60° was recently notified [13].

2.1.8 Vortex shedding

Rediniotis, Stapountzis and Telionis [13] measured the wake region velocities of the delta wing. Existence of vortex shedding was shown at high AoAs. In addition, existence of both symmetric and anti-symmetric modes of shedding was found. Based on experiments on delta wings with a sweep angle of 76°, vortex shedding, which is a quasi-periodic happening, takes place in the broad range of AoA with insignificant influence of Reynolds number. While only symmetric mode of vortex shedding occur up to 70° AoA, symmetric (more dominant mode) and anti-symmetric vortex shedding modes exist simultaneously. Studies of Gursul et al. [13] on the transition between helical mode instability and vortex shedding were accomplished and it was found that helical mode instability vanishes after vortex breakdown comes to the tip of the wing with the emergence of dominant frequency of vortex shedding. From helical mode instability to shedding of the vortex sudden transition indicated by frequency jump in Figure 2.6, occurred at the AoA at which vortex breakdown arrived the tip of wing. Figure 2.7 shows the dimensionless frequency spectrum of unsteady flow phenomena over delta wings [13].

2.2 Previous Studies on 70° Delta Wing Studied in the Thesis

In this part, previous experimental and numerical studies on 70° delta wing are summarized. It is important to note that experimental studies of Mitchell [19, 20, 21] given in this section are used for the validation of the current CFD model. For that purpose, investigations on these studies are given in detail. After the summary of Mitchell's experimental studies, previously conducted CFD studies related with Mitchell's study are presented.

2.2.1 Experimental studies

Experiments were performed at Onera F2 subsonic wind tunnel. This wind tunnel is a closed-return atmospheric tunnel having a rectangular test section whose width of 1.4 m, height of 1.8 m and a length of 5 m. Freestream velocity in the test section can reach up to 105 m/s and estimated accuracy of the relative freestream velocity $\Delta U_0/U_0$ is 1 %. Mean intensity of turbulence is 0.1 % in the wind tunnel [19, 20]. Constant freestream temperature in the test section is provided by a cooling system in the closed-return part. All of experimental studies were achieved at atmospheric conditions. AoA of delta wing that was assembled on a sting has an accuracy of 0.05° (Figure 2.9). In addition, delta wing was placed in wind tunnel such that yaw angle was not present with respect to direction of the freestream flow with ± 0.1° predicted accuracy [20, 21].

In order to get qualitative and quantitative data, two delta wing models were used. The model deprived of instrumentation mounted on surface was utilized to acquire flow field. Steady surface pressure data was collected by second model with 232 pressure taps with a diameter of 2 mm and the taps were longitudinally located at 16 sections in order. Measurement methods including laser sheet visualization, surface oil flow, surface pressure and three-dimensional Laser Doppler Velocimetry (LDV) were utilized to completely understand the flow field [20, 21].

The ensemble of the laser sheet images were used to describe the physical location of the leading edge vortices and breakdown location of the vortex [19, 20] (see Figure 2.10). According to Guy et al. [22], the angle between the core of the vortex and the upper side of the delta wing depends on AoA. Approximate value of this angle is 0.26×AoA. Experimental results showed that this angle is 7° at an AoA of 27° and this result confirms the statement of Guy et al. [22]. Each vortex core follows a path starting from wing apex and follow along a sweep angle of 77° until reaching the trailing edge where it turns in the direction of the freestream velocity.

From recorded laser sheet images, the streamwise distance of the vortex breakdown location (X_b) was measured directly. The ratio of the measured vortex breakdown location to the root chord length (c) provides the non-dimensional term (X_b /c). When X_b /c equals to 1, it means that vortex breakdown takes place at the trailing edge. Blue circles in Figure 2.11 represent the vortex breakdown locations, at wide range of AoA, specified from laser sheet images that are perpendicular to the upper side of the delta wing. A recorded history of the vortex breakdown locations were provided by the video data obtained at AoA of 27°. In order to specify the mean vortex breakdown locations, averaging of frame by frame analysis of 1500 data points were achieved. Center of error bars depicted in Figure 2.11 show mean vortex breakdown locations of both side (starboard and port). Moreover, top and bottom values of these error bars demonstrate extreme values of the vortex breakdown locations in each of data sets.

It is confirmed by the usual behavior in Figure 2.11 that location of the vortex breakdown shifts from trailing edge to wing apex as AoA is increased. According to Mitchell's study [19, 21], the time-averaged location of the vortex breakdown was found to be approximately X = 620 mm (X_b / c = 0.65). Variation of vortex breakdown position around mean position is ± 0.05 according to error bars given in Figure 2.11.

By analyzing the oil strake topology with the help of critical point theory, correlation between skin friction pattern of the leeward surface and the flow field could be obtained [21]. Figure 2.12 shows the surface oil flow visualization. Reference grid remarks the chordwise positions on the top surface of the delta wing. X = 200 mm is the very first line. The distance between successive line is 100 mm and the final reference line is located at X = 900 mm (see Figure 2.12).

Because of the sharp leading edges of the model, the primary separation lines are fixed at the leading-edges so that it is hard to recognize in the oil flow visualization. Primary attachment lines are noticeable on the leeward surface. The

borders of green and red colors near the leading edges are the location of the secondary separation lines.

Figure 2.12 shows a rapid change in the direction of secondary separation line. This indicates that laminar to turbulent transition between X = 360 mm and X = 380 mm takes place. Secondary separation lines, located at quite inboard of the leading edges in the beginning, drastically located outward hence approached to leading edge. The reason of shifting of secondary separation line is because turbulent boundary layer resists more to separation than the laminar boundary layer. Due to the more resistance of the turbulent boundary layer to separation, the distance between the primary attachment and the secondary separation lines increases [21]. As the AoA is augmented, this transition division has a tendency to move upstream [19].

It was seen from steady state surface pressure measurements that suction peak were observed at 66 % of the dimensionless location of the wingspan (Y / b). Minimum magnitude of pressure coefficient was placed close to the wing tip (apex). Figure 2.13 shows the Cp contour of the upper side of the delta wing at AoA=27° and freestream velocity of 24 m/s. Figure 2.12 also shows the influence of the leading edge vortices on the leeward surface of the delta wing. Nevertheless, Cp contour did not reveal any significant changes nearby the mean vortex breakdown location [21].

Only port side of the flow field was investigated with LDV due to the symmetry of the flow field. Four planes perpendicular to the leeward surface of the delta wing were examined with LDV measurement method: X = 500 mm zone where leading edge vortex well developed, X = 600 mm regions just upstream of the breakdown, X = 700 mm region downstream of breakdown and X = 800 mm zone where the flow is disorganized [21].

Figure 2.14 reveals the dimensionless longitudinal velocity (U / U_∞) measured at four planes. A jet like flow ($U / U_\infty \geq 3.5$) in core of the vortex is clearly seen prior to vortex breakdown (X = 500 mm and X = 600 mm) [19, 21]. For the planes

located at X = 700 mm and X = 800 mm where the breakdown already happened, negative dimensionless longitudinal velocity along the remarkably expanded vortex core is examined. Vortex core velocity turns from jet like profile at upstream of breakdown to wave like profile at downstream of breakdown.

Figure 2.15 presents the axial vorticity at four perpendicular planes. There are two significant regions needed to be paid attention. One is highly negative vorticity in the core of the vortex while second zone is vortical substructures in the shear layer detached from the primary separation line. In the time averaged data, these vorticity pockets are evidently identified and have a similar evolution to Kelvin Helmholtz instability. Dissipation of the vorticity in the vortex core indicates that vortex breakdown has already occurred (X = 700 mm and X = 800 mm of Figure 2.15). Yet, the vortical substructures still appear both prior to the breakdown and after the breakdown. Moreover, positive sign of the vorticity close to the leading edge is the evidence of secondary vortex [21].

Non-dimensional turbulent kinetic energy (TKE = k / U_∞^2) contour is presented in Figure 2.16. Due to very nature increase of fluctuations at oscillating vortex breakdown region, magnitude of turbulent kinetic energy at X = 700 mm plane is high. Level of TKE at X = 800 mm is not as high as X = 700 mm but still high compared to upstream of vortex breakdown region because of highly disorganized flow field.

In Figure 2.17, non-dimensional axial velocity along the core has a jet like profile prior to the vortex breakdown similar to Figure 2.14. Then, there is a rapid deceleration of the core velocity and enlargement of the vortex core followed by the recirculation zone. In Figure 2.18, there is remarkable increase in magnitude of TKE at stagnation point and just after the location of the vortex breakdown.

2.2.2 Numerical studies

J.-F. Le Roy et al. [23, 24] carried out both steady and unsteady computations over 70° sweep delta wing with sharp leading edge. Half span delta wing was used for the simulations. Dimensions of the simulation domain were 4 Root Chord (RC) upstream, 6 RC downstream, 5 RC up, 5 RC down from wing apex and 4 RC away from wing centerline. Mesh with 3,030,081 number of points and around 4 million of cells were employed for the steady and unsteady simulations respectively. Steady simulations were performed with elsA software while unsteady computations were achieved at FLU3M software. Since Mach number has been taken as 0.2, chord of the delta wing was shortened 0.34 m in order not to alter the Reynolds number which was 1.5 million. Symmetry boundary condition was used for the symmetry plane, no slip and adiabatic boundary conditions were used for the walls. The Spalart-Allmaras-rotation correction (SARC) and Menter's Shear Stress Transport turbulence models were used. Findings were compared with Mitchell's experimental study. Steady SST model predicted the vortex breakdown location at 75 % of the wing chord while steady SARC model predicted 93 % of the wing chord. It is 70 % in the DES simulation. Peak velocity at the center of the leading edge vortex was approximately 2.5 times the freestream velocity in steady state calculations [23]. It was 3.5 times the freestream velocity at the experiment as previously discussed. Turbulent kinetic energy contour showed 5 times lower magnitude than experimental value. Pressure coefficient (Cp) at leeward surface beneath the leading edge vortices and non-dimensional axial velocity values were also underestimated. DES and steady SST approach showed similarities such that both simulations produce strong secondary vortex that causes low intensity of the primary vortex and relocation of the primary vortex more inboard of the delta wing [1].

Morton et al. [25] compared both RANS models including SA, SARC, SST and DES models including SADES and SSTDES with each other and experimental data. 2.45 million unstructured grid was generated for computations. Simulations

were performed with Cobalt solver. All cases were carried out at same Reynolds number, Mach number, free stream velocity and AoA as in the experiment. Axial vorticity, breakdown location and TKE values were compared.

It was clearly stated that too much eddy viscosity that kills the resolved turbulence kinetic energy is added to vortex core by typical RANS models (SA, SST) so that location of the vortex breakdown is not successfully captured. On the other hand, both DES methods and Spalart-Allmaras rotation correction model (SARC) offer comparable results with experimental data. Difference between SARC and SA is an additional destruction term that was included in the simulation to limit the production of eddy viscosity in regions with high vorticity.

Soemarwoto et al. [26, 27] performed URANS simulation and compared results of the simulation with experimental data. Since standard RANS methods produce excessive level of eddy viscosity resulting excessive dissipation in the vortex core, a modification to k-w turbulence model were achieved. With this modification, production of the turbulence kinetic energy was controlled through promoting the production of the dissipation rate. ENFLOW software was used for the simulation. 3,694,080 cells were generated for the flow domain. In the simulation; Mach number, AoA, Reynolds number matched with experiment. While Cp distributions gave qualitative agreement with experimental data, suction peaks were underestimated. Underestimated magnitudes were also seen at velocity contours. Vortex breakdown location was found to be at X_b / c = 0.74 in the simulation. It was shown that that high vorticity inside the primary vortex before breakdown and vorticity pockets trailing from the shear layer were not captured by the simulation. However, axial vorticity levels after breakdown were comparable with experiment. It was stated that calculated TKE was one order of magnitude less than the experiment.

Second series of experiments were accomplished by Mitchell et al. [15] because of wide spacing between perpendicular planes of data showed at the experimental studies section. Figure 2.19 demonstrates the non-dimensional axial vorticity at

various planes (in total 14) perpendicular to the upper side of wing. It was seen that there are vortical substructures around vortex core and they revolve around vortex core as they are evolving in the direction of the trailing edge. Axial component of vorticity in substructures is the same order of magnitude of longitudinal component of vorticity in the vortex core. It was also observed that as X/c is increased, magnitude of the vorticity in the axial component decreased. It was stated that this proportion is the indication of the existence of local instability close to the primary separation line (leading edge) that generates the substructures. Moreover; in the separated shear layer, co-rotating and stationary substructures were confirmed by the ensemble of 3-D LDV results. Nevertheless, findings of that experiment do not evaluate precisely instability mechanism causing the forming of the substructures. Computational effort needed to provide more precise flow field analysis and to assess the hypotheses related with many instabilities observed experimentally. Time accurate CFD simulations were performed to get more information about instability and forming of the substructures. Dimensions of the domain was: 10 m upstream and 10 m downstream, 5 m spanwise, 5 m up and 5 m down from wing apex. AoA, Reynolds number, Mach number at DES matched with experiment. Cobalt solver was used. DES accurately resolved these vortical substructures. It was stated that capturing these substructures highly depend on grid density. Mitchell et al. [15] observed two different substructures; one is stationary and the other is time varying.

S.Görtz [28] performed DES in order to simulate flow field over full span delta wing. Dimensions of the simulation domain was 4 RC upstream, 6 RC downstream from wing apex, 4 RC below and above the wing and 4 RC span wise in both port and starboard directions. 4,231,936 finite volume cells were used for the simulation. Navier-Stokes Multi Block (NSMB) software was used. Solutions were achieved for Mach number 0.2, AoA = 27°, Reynolds number 1.56×10^6. AoA and Reynolds numbers were taken same with experiments. Mach number was changed to 0.2 in order to diminish stability problems. Vortex breakdown location range was found to be $0.769 < X_b/c < 0.797$ for the starboard and $0.789 < X_b/c < 0.813$

for the port side. Asymmetry in breakdown location between port and starboard side indicated that full span DES could provide interaction of port and starboard vortices. Qualitative agreement like suction peak locations between simulation and experimental results were seen at surface pressure distribution but magnitude of suction peak (Cp) and velocities in contour plots were underestimated. In the paper, possible reasons of this underestimation could be due to grid resolution and/or wind tunnel blockage effects that could cause higher effective angle of attack. Therefore, further simulation was performed by refining grid following results were obtained: Suction peak was insignificantly increased. The longitudinal component of velocity contour U/U_∞ showed better resolution of vortex core when compared to previous simulation. Better resolution of vortex core leads to better agreement of vortex breakdown location with experimental data. Secondary vortex surface pressure peak that experiments failed to capture was seen in simulation.

Allan et al. [1, 29] worked on effect of wall influences on delta wings. Several turbulence models were investigated and modified k-ω turbulence model was used for the wall tunnel interference studies. Modified k-ω turbulence model was selected to eliminate excessive eddy viscosity within vortex cores. Firstly, grid dependency study was conducted. It was seen that suction peak and vortex breakdown location depended on grid resolution. Breakdown locations for coarse and standard grids were 59.6 % and 64.7 %, respectively. 3,969,810 cells were used for simulations. In the simulation, Reynolds number, AoA matched with experiment whereas Mach number was changed to 0.2 in order to avoid convergence problems. For the validation, results were compared with ONERA F2 tunnel experiment. It was concluded that side wall proximity cause vortex breakdown location to move upstream. In other words, wall proximity promotes vortex breakdown. Effects of wing support were also analyzed. Influence of support to flow increases as the support positioned closer to the trailing edge.

Moigne and Rizzi [30] conducted grid study of a 70° sweep delta wing. No wake, a short wake and full wake refinement studied with 668,000, 1.8 million, 4.4 million mesh cells respectively. Half span delta wing was used for the simulations.

Domain extended from apex to 4 RC upstream, 4 RC above, 6 RC downstream, 6 RC below and 6 RC spanwise directions. Unstructured EDGE solver was used for the EULER (inviscid) simulations. Vortex breakdown locations were found to be at 54.7 %, 62.5 %, and 61.4 % of the chord for no wake, short wake, and full wake refinement respectively. It was unfortunately assessed that no trend was captured at refinement study except that no wake refinement predicted vortex breakdown far upstream.

Scott Morton (2009) [31] also worked on SADES and compared the results with experimental data and previously conducted CFD results. Reynolds number, AoA and Mach number matched with experiment. Cobalt solver was used for the simulations. It was seen that as the grid density increases, number of resolved eddies increase and that study also showed the previously known fact that vortex breakdown position relies on resolution of the domain. Surface pressure coefficients were underestimated as in previous CFD studies and 24 % peak difference was calculated between simulation and experimental data. Computed peak pressure difference between experimental data of Görtz's study [28] at 500 mm was 23.8 %. It was 22.4 % at Soewarmoto et al.'s URANS study [26, 27] and 23.8 % at LeRoy et al.'s RANS study [23, 24]. It was also pointed out that possible source of this difference between experimental data and all conducted CFD studies could arise from the dynamic pressure scaling. TKE contour at a plane passing through vortex core and situated parallel to delta wing surface was analyzed. Magnitude and location of TKE were well predicted at post breakdown region whereas pre breakdown region was not predicted such that produced TKE was not observed in the vortex core. Previous solutions obtained so far were simulated as fully turbulent flow. However; on the leeward side of the delta wing, laminar to turbulence transition exists at 40 % of chord in the experiment. So this transition issue was simulated by zeroing the production of eddy viscosity through the upstream of 40 % root chord. Extra case was provided by zeroing the production of eddy viscosity through the upstream of 30 % root chord. It was shown that transition simulation causes the generation of TKE in the core before

the breakdown and modification also affects the surface oil patterns so that transition could be observed.

2.3 Vortex Breakdown Flow Control Mechanisms on Delta Wings

As mentioned before, swirl level and the pressure gradient outside of the vortex core are the two important factors affecting vortex breakdown. It was mentioned that ratio of swirling velocity (V_θ) to the longitudinal velocity (V_z) cannot exceed the value approximate to 1.3 at any point of the profile [32]. Vortex breakdown will take place, if this ratio (also called swirl number) goes beyond 1.3.

Helix angle ($\gamma=\tan^{-1}(V_\theta / V_z)$) is another expression of this fact and this angle cannot exceed 50° [10]. Pressure rise retards the longitudinal motion and hence causes an augmentation in swirl number which leads to the onset of vortex breakdown. Contrarily, a favorable pressure gradient decrease swirl number and stabilizes the vortex.

Depending on the considered application, vortex breakdown phenomenon can be advantageous or disadvantageous. For instance; vortex breakdown phenomenon is beneficial when the intent is to improve the mix of fuel and air in a combustion chamber. Conversely, vortex breakdown is being characterized as an origin of performance loss over highly swept aircraft at high AoA. Since vortex breakdown generally occur asymmetrically over wings, the difference in lift loss can stimulate a roll moment distorting aircraft stability [32].

Since vortex breakdown phenomenon is closely linked to the swirl number, any attempt to increase the longitudinal component V_z or slow down the tangential component V_θ decrease the swirl number and hence delay vortex breakdown. Mechanical or pneumatic devices can be used to control swirl number. In this section, pneumatic control mechanisms over highly swept delta wings, especially along-the-core blowing technique is mainly discussed.

Werle [32] began with applying several control methods by conducting experiments to alter the breakdown location of vortex. Four vortex breakdown control techniques including obstacle located downstream of the flow, trailing edge suction, along-the core-blowing and flow ejection counter to vortex core were applied to 60° sweep delta wings with sharp leading edges in the experiments as shown in Figure 2.20. Werle showed that positioning of obstacle in the downstream flow (close to trailing edge) promoted vortex breakdown and moved the vortex breakdown position to upstream. Similarly, blowing counter to vortex core also moved the vortex breakdown location further upstream. On the contrary, Werle demonstrated that along-the-core blowing on the suction surface and suction around trailing edge moved the location of the breakdown further downstream or got rid of the vortex breakdown. Werle also observed that the position of the vortex core moved to align with along-the-core blowing jet. In order to evaluate the magnitude of flow input by blowing, the dimensionless term, "momentum coefficient", was introduced. To retard the vortex breakdown location significantly by steady along-the-core blowing, the magnitude of the C_μ was observed to be around $10^{-3} < C_\mu < 10$. Werle also mentioned that AoA, sweep angle, shape of the leading edge and thickness of the wing were the parameters that determine the effectiveness of steady and unsteady control [32].

Mechanical equipment and pneumatically driven techniques are the primarily two broad categories of the control of flow field over delta wings. Mechanical equipment includes canards, flaps, fillets, leading edge extensions (LEXs), strakes, and vortex fences. Pneumatically driven control techniques encompass various configurations of suction and blowing which are tangential blowing, suction along the vortex core, spanwise blowing, trailing edge blowing, along the vortex core blowing, leeward surface suction and leading edge suction. Combinations of mechanical and pneumatic methods are also utilized to control vortical flow [32].

2.3.1 Mechanical devices

Canards were utilized for Saab Viggen to retard the vortex breakdown on the main delta wing so that performance of aircraft at higher angles was maintained. Likewise, LEXs has been mounted on the fighter aircrafts. Lamar et al. experimentally analyzed the strake variables including planform shape, slenderness and semi-span on the flow field [32].

Rao [32] conducted series of experiments on 60° and 74° delta wings and primarily analyzed the influence of flaps. According to his findings, the ratio of lift to drag can be enhanced up to 18.4 % by flaps. Marchman [32] obtained the same observation of Rao by working on delta wings having 60° and 75° sweep angles. Influence of flap size in enhancing the lift was demonstrated by comparing various flap geometries. Influence of simultaneous use of leading and trailing edge flaps on the vortex flow was analyzed by Marchman et al. [32]. Rao et al. [32] and Klute et al. [32] studied on apex flap. Wahls et al. [32] studied the influence of apex fence, which is a panel placed in the tip of the delta wing, on the flow field. It was shown that upper surface suction level is improved approximately 10 % when compared to nominal case. Schaeffer et al. [32] worked on leading edge cavity flap design in order to control the vortical flow around 75° delta wing at an AoA equal to 35°. It was concluded that leading edge vortices move inboard and vortex breakdown was delayed. Schaeffer et al. [32] conducted further investigations by expanding cavity flap. Benefits of cavity flaps in steady flows are more pronounced. Gursul et al. [32] worked on leading edge oscillating flaps and investigated the mechanical system enable the change of sweep angle of delta wing from 60° to 70° as shown in Figure 2.21.

Gursul et al. [32] stated that since leading edge vortices were formed by the separation of the flow along the leading edge (primary separation line), devices positioned at the leading edge were prominent tools to control the vortical structures. It was noted that effectivity of leading edge flaps on the vortex flow

depends on AoA. Moreover; adjusting sweep angle of the model, vortex breakdown location could be altered. Vorobieff et al. [32] investigated the simultaneous effects of leading and trailing edge control methods by testing each method separately and testing with various combinations aiming to delay vortex breakdown with least energy entrainment from control techniques.

2.3.2 Pneumatic techniques

As mentioned previously, studies of Werle [32] investigated the initial tests to control vortical flow field by pneumatic flow control methods. In addition, factors like flow input of suction or blowing (usually characterized by momentum coefficient, C_μ), continuous/pulsed suction or blowing and wing/flight conditions (sweep angle, AoA, wing thickness, shape of the leading edge etc.) were also demonstrated to play a role in the effectiveness of pneumatic control techniques.

Parmenter et al. [32] showed that applying the localized suction constantly at around downstream of the breakdown location displaced breakdown location closer to the trailing edge. Moreover, influence of non-dimensional suction coefficients $(Vs / U_\infty)^2 (A_s / S_{wing})$ ranging from 0.035 to 0.57 to the shifting of the vortex breakdown were observed and concluded that as the distance between vortex breakdown location and the suction device decrease and then smaller suction coefficients became effective. McCormick et al. [32] experimentally investigated the leading edge suction and the suction located at more inboard of the leading edge on delta wings having sweep angle of 65° and 70°. Modification of shear layer and leading edge vortical structures were caused by suction near the separation point. Moreover, vortex breakdown was retarded significantly by leading edge suction and shifting of the breakdown position increased with the augmentation in suction coefficient. Suction was also accomplished asymmetrically around one leading edge and it was revealed that uncontrolled vortical structure does not change. Qualitative results of Maines et al. [32] showed

that the relationship between the coefficient (related with momentum of suction and freestream velocity) and vortex breakdown location is linear.

Helin et al. [32] conducted water tunnel experiment with 60° sweep delta wing in order to investigate the effect of jet flow entrainment through trailing edge on the position of the vortex breakdown. Various velocity ratios (jet exit velocities to free stream velocity) ranging from 0 to 8 were examined and dramatically different breakdown locations were observed with different velocity ratios. With a velocity ratio of 8, vortex breakdown location was delayed up to 18 % of the chord. Nawrocki [32] used the same delta wing configuration and velocity ratio range as Helin [32]. In his study, jets located at trailing edge were oriented ± 45° with respect to trailing edge of the wing. It was observed that thrust vectoring moves the position of breakdown 40 % of the RC with 45° jet deflection and velocity ratio of 8. Shih and Ding [32] conducted experiments with 60° sweep delta wing in order to examine trailing edge blowing (velocity ratio ranging from 0 to 7.3) control for both static and pitching conditions. Results showed that downward jet angle of 45° with highest blowing coefficients moves the nominal breakdown location further downstream by 58 % of the root chord. It was stated that adverse pressure gradients primarily responsible for vortex breakdown were eliminated by jet entrainment near the trailing edge. Vorobieff and Rockwell [32] studied on pulsed trailing edge blowing and they concluded that intermittent blowing was much more efficient than continuous blowing. Mitchell et al. [32] worked on controlling a 75° sweep delta wing with asymmetric and symmetric trailing edge jet injection. Findings confirmed the previous results. However, blowing through the trailing edge with velocity ratio of 15, which is the highest value, moved the vortex breakdown location to upstream toward wing apex because high velocity ratio jets behaved like an obstacle and this provoked adverse pressure gradient.

Alexander [32] worked on along the leading edge perpetual blowing of a 70° swept delta wing. “Blowing coefficient of momentum ($C_\mu = Q_m V_j / q_\infty S_{wing}$)” term was defined by Alexander [32]. In order to evaluate the momentum entrained to

flow field by blowing, this term is mostly used. Trebble [32] performed experiments on 70° delta wings with blowing along the leading edges. Dixon [32] and Cornish [32] worked on spanwise blowing in order to achieve lift augmentation and they concluded that jets having high pressure or nozzle with small exit area were more effective because of leading high jet exit velocities and lift augmentation ratios between 2 and 5 were reached. The lift augmentation does not solely depend on the blowing momentum coefficient but also depends on jet velocity to freestream velocity ratio. Bradley et al. [32] examined controlling the half span and high swept aircraft in compressible flow regime by blowing to leading edge in a parallel direction and this technique improved both lift and drag. Seginer and Salomon [32] also studied on jets that were oriented parallel to the leading edges of 60° sweep delta wing (Mirage IIIC). Blowing not only increase the maximum lift but augmented the lift-curve slope at the same time. Wood et al. [32] investigated tangential leading edge blowing technique on the half delta wing having 60° sweep angle. It was concluded that direct control of primary separation is a powerful way to control vortical flow field. Roberts and Wood [32] investigated tangential leading edge blowing utilizing the coanda effect.

2.3.2.1 Along the core blowing

Afchain et al. [32] and Laval-Jeantet [32] studied on controlling the 70° swept delta wing by along-the-core blowing. Location of the jet was at 14 % of the RC and located underneath the vortex core. Results demonstrated that along-the-core blowing was capable of displacing the mean vortex breakdown location closer to trailing edge. Miller and Gile [32] accomplished experiments in order to investigate along- the-core blowing both close to the tip and along the centerline of the wing. Kuo et al. [32] performed tests to examine transient along-the-core blowing with momentum coefficient ($C_\mu = (V_j / U_\infty)^2 / (A_j / S_{wing})$ of 0.088 (blowing slot diameter of 0.5 mm) over 70° sweep half delta wing with an AoA of

40°. It was noted that along the core blowing was more effective on the vortex core prior to vortex breakdown. It was also noted that since vortex core prior to breakdown served as "transmitting vessel" meaning that supplied momentum delivered steadily to beat the unfavorable pressure gradient. Changes in axial and swirl velocity under applying transient along the core blowing were researched by Kuo and Lu [33]. Magnitude of longitudinal velocity increased with blowing then decreased right after the end of the pulsed blowing. On the other hand, swirl velocity component does not change with and without along the core blowing.

Guillot et al. [34] performed experiments with half delta wing having 60° sweep angle to investigate blowing momentum coefficient, optimum location and blowing angle of the jet for along-the-core blowing control method to retard breakdown of the vortex. Five nozzles having a diameter 1.6 mm were located beneath the vortex core as shown in figure Figure 2.22. Nozzles were capable of emitting jets at pitch angle varying from vertical to 45° from the horizontal. Nozzle located at 30 % of the RC (closest location to wing tip) was found to be the most effective position. It was also noted that pitch angle of 45° was most effective among the available angles. Figure 2.23 shows the performance of blowing as a function of azimuthal angle with constant blowing coefficient (C_μ = 0.01). In this figure; while θ = 180° represents the blowing in the direction of free stream, θ = 90° represents the direction pointing normal and away from the fuselage. Optimum azimuthal angle is not vortex core azimuth angle 158° but it is closer to 180°. Flow visualization showed that a jet initially vectored to the along the core was deflected towards leading edge because of the tangential velocity of the vortex and for this reason, it was less effective. In other words, a jet initially oriented towards fuselage was then brought to vortex core by tangential flow and showed the most effective performance. If the jet is oriented beyond 180°, decrease in performance was seen, especially at higher flow rates. Figure 2.24 demonstrates the relationship between breakdown location and blowing momentum for three azimuthal angles. Decrease in performance of high blowing momentums beyond 180° was also seen in that figure. Drop off in performance arise from the fact that

jet is blowing inboard instead of vortex core. On the contrary; unless its momentum was very high, nozzle rotated at 160° (just inboard of the vortex core) deflected outboard of the vortex core because of tangential velocity. Azimuthal angle of 170° was the most effective azimuthal angle and vortex breakdown was retarded from 55 % of the RC to the trailing edge as seen from Figure 2.24.

Optimum location in order to maximize the control and to minimize the entrained flow was reported to be near the leading edge and close to the apex by Visser et al. [35].

2.3.2.1.1 Along the core blowing on 70° swept delta wing studied in this thesis

Mitchell et al. [36-38] performed experiments on 70° swept delta wing to examine effect of the along the core blowing on the breakdown position of the vortex. Two Blowing nozzles were situated symmetrically at 14 % of the RC and at a distance of 30 mm from the leading edge.

Circular Jets were discharged from diameter of 2.07 mm into an open duct at an angle of 15.6° with respect to upper surface. In addition, two nozzles were oriented a little inward of the primary vortex cores (5°) by taking into consideration of the study of Gulliot et al. [34]. Momentum coefficients (C_μ) of 0.004, 0.005, 0.0057 and 0.006 with corresponding mass flow rates of 1.4, 1.8, 2 and 2.2 g/s were examined at test conditions of $U_\infty = 24$ m/s ($Re = 1.56\times10^6$) and AoA of 27°.

As previously mentioned, vortex breakdown location was at $X_b / c = 0.65$ without blowing case. Breakdown locations (X_b / c) were identified at 0.72, 0.78 and 0.95 for the blowing cases of 1.4 g/s, 1.8 g/s and 2.2 g/s, respectively. As a conclusion, it was stated that along-the-core blowing does not change the characteristics of vortical structures prior to vortex breakdown. This control technique basically

augments the momentum of vortex core to overcome the unfavorable pressure gradients.

2.3.3 Numerical studies on the control of leading edge vortices

Kyriakou et al. [39] worked on numerical modeling of vortex breakdown with and without a trailing edge jet flap using commercial code Fluent and good agreement with experimental data of Shih et al. [40] was observed. Vlahostergios et al. [41] also worked on modelling of experimental work of Shih et al. [40] with in house Navier-Stokes solver utilizing linear and nonlinear eddy viscosity turbulence models and concluded that results of non-linear models were closer to experimental data.

Jinsheng Cai et al. [42] aimed to evaluate efficiency of series of leading edge vortex flaps on nonslender delta wing both numerically and experimentally. Satisfactory agreement observed between PIV results of uncontrolled wing and numerical results.

Cummings et al. [43] studied on 70° sweep delta wing examining periodic blowing and suction control by unstructured flow solver Cobalt. It was noted that effect of periodic suction and blowing on flow field was properly captured and this study enabled researchers to further investigate the flow field information that was not recognized from tests like breakdown of the vortex frequency on winding and incremental alteration in normal force due to periodic suction and blowing.

Jacop A. Freeman [44] worked on numerical investigation of vortex breakdown and along the core blowing of 60° sweep delta wing utilizing various turbulence models including Spalart-Allmaras (SA), Renormalization Group k-e, Reynolds Stress Model (RSM), and Large Eddy Simulation (LES) with FLUENT code. Results of his research showed that none of turbulence models except LES for

which mesh was not sufficiently refined and was not investigated in detail, gave comparable solution to the experimental data.

Muramatsu et al. [45] carried out numerical computations by FLUENT 6.1 to examine effective blowing direction on a delta wing to avoid vortex breakdown and to increase lift. For that purpose, many combinations of blowing azimuthal and pitch angles were analyzed. It was concluded that blowing in the direction of span was ineffective and pitch angle between 30° and 60° were shown to be effective delaying vortex breakdown location.

S. Chung et al. [46] conducted CFD simulations with FLUENT 6.3 on the variable geometry strake that generate combinations of both co-rotating and counter-rotating vortex pairs as an active flow control and results indicated a great change in aerodynamic forces with counter rotating vortex pair.

To sum up, there are many techniques to control leading edge vortices. Figure 2.25 demonstrates the effectiveness of these blowing/suction control techniques by introducing the term $(\Delta X_{bd} / c) / C_{\mu}$ where ΔX_{bd} is the change in breakdown location, c is the root chord and C_{μ} is the momentum coefficient. According to Figure 2.25, along the core blowing is the most effective method in order to delay vortex breakdown. Moreover, Figure 2.26 compares the steady and unsteady blowing in terms of $\Delta C_N / C_{\mu}$ where ΔC_N is change in normal force coefficient and C_{μ} is momentum coefficient. It is seen that unsteady blowing is having a great potential for active flow control [47].

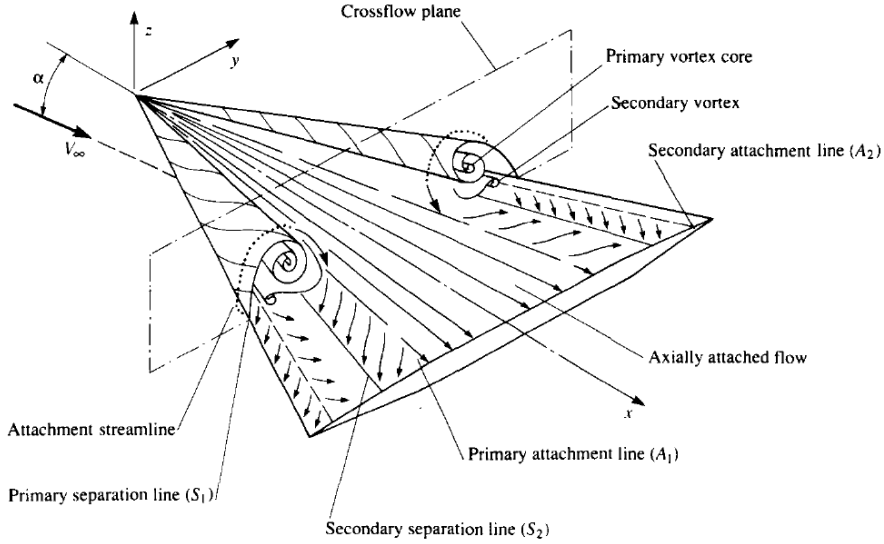

Figure 2.1 Schematic of the flow field over the leeward surface of delta wing at angle of attack [3]

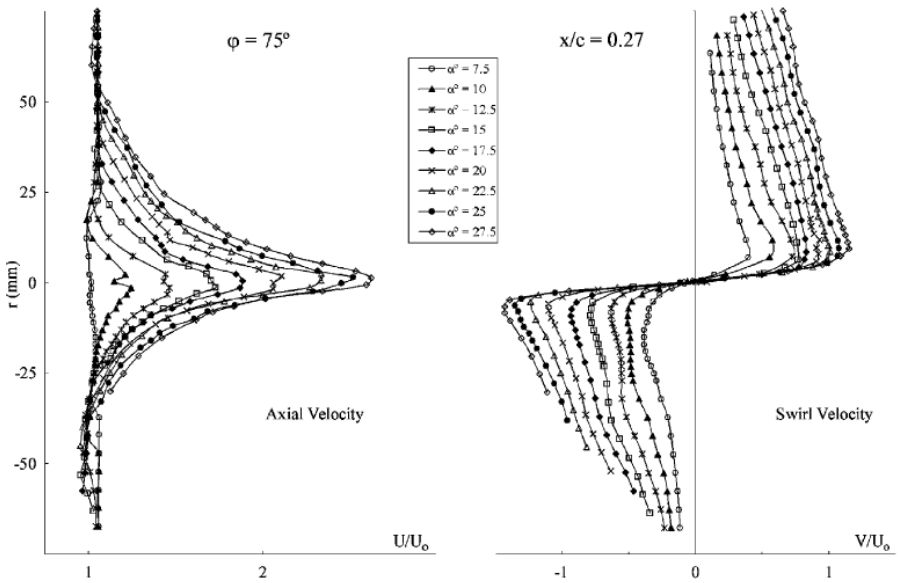

Figure 2.2 Velocity distribution in the vortex core before breakdown [4]

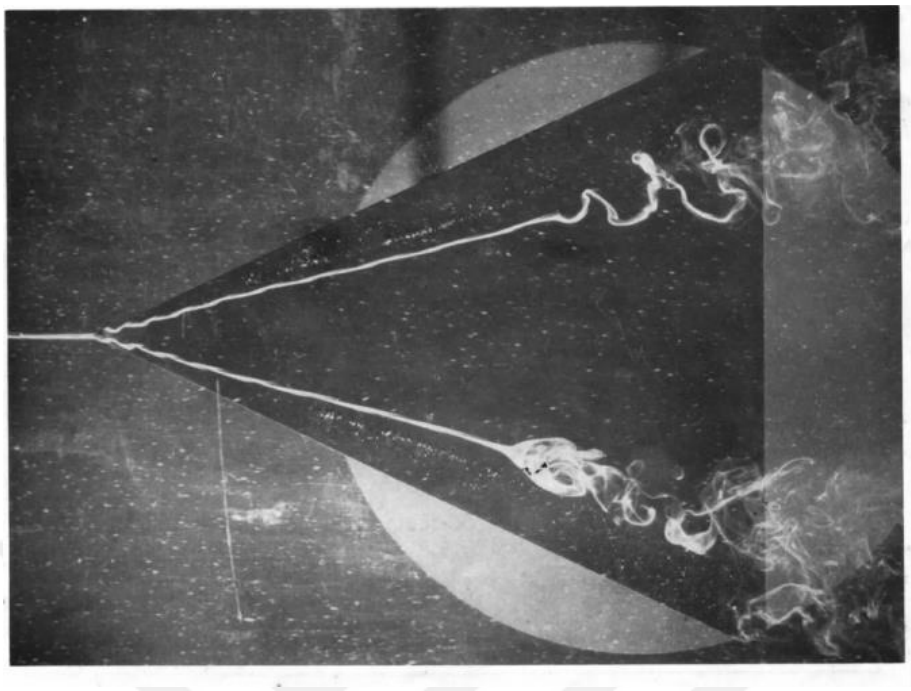

Figure 2.3 Spiral and bubble type vortex breakdown [7]

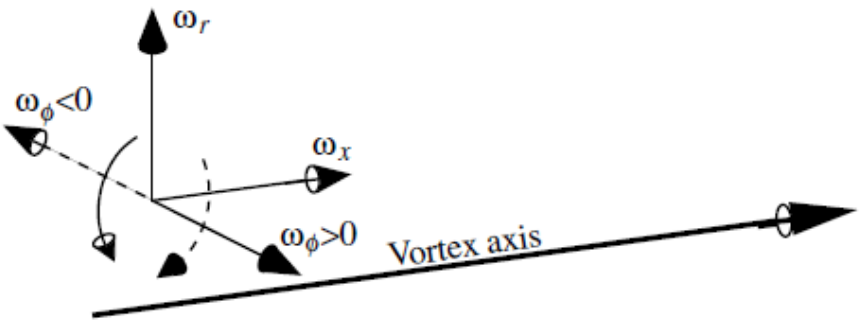

Figure 2.4 Sense of azimuthal vorticity [12]

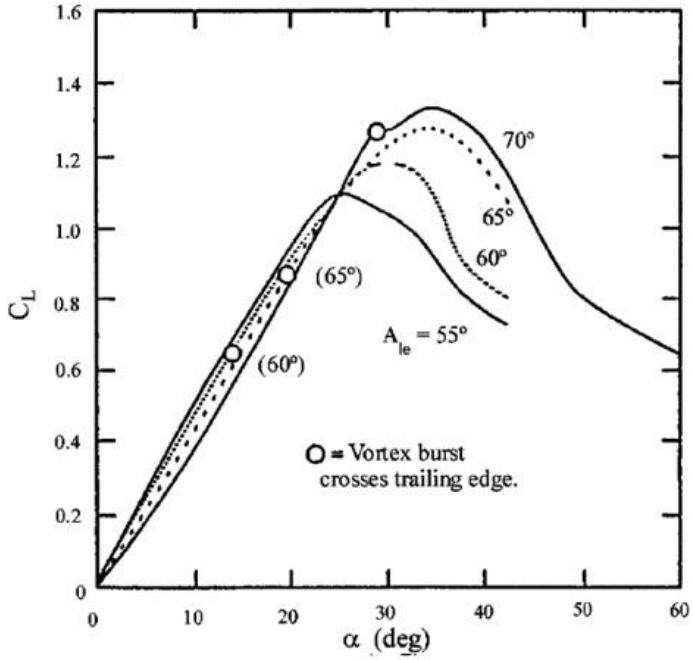

a)

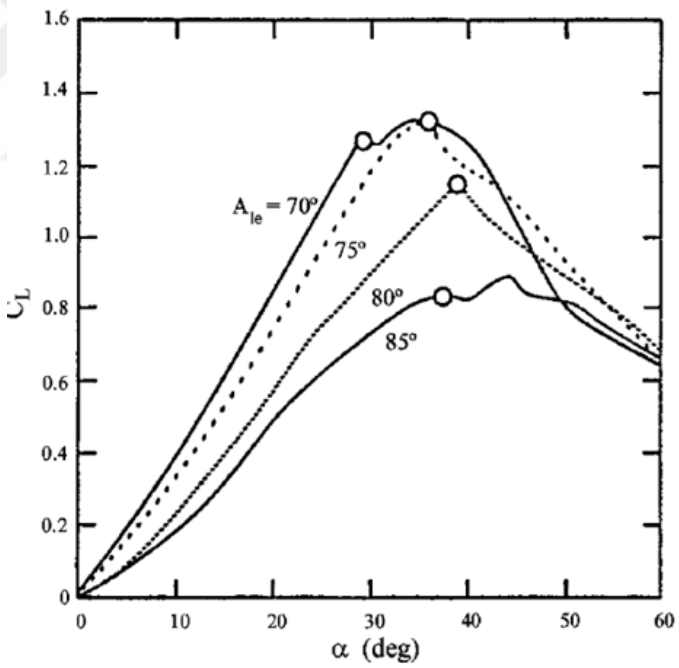

b)

Figure 2.5 Lift coefficients for flat plate delta wings having sweep angle between a) 60° - 70°, b) 70° - 85° [4]

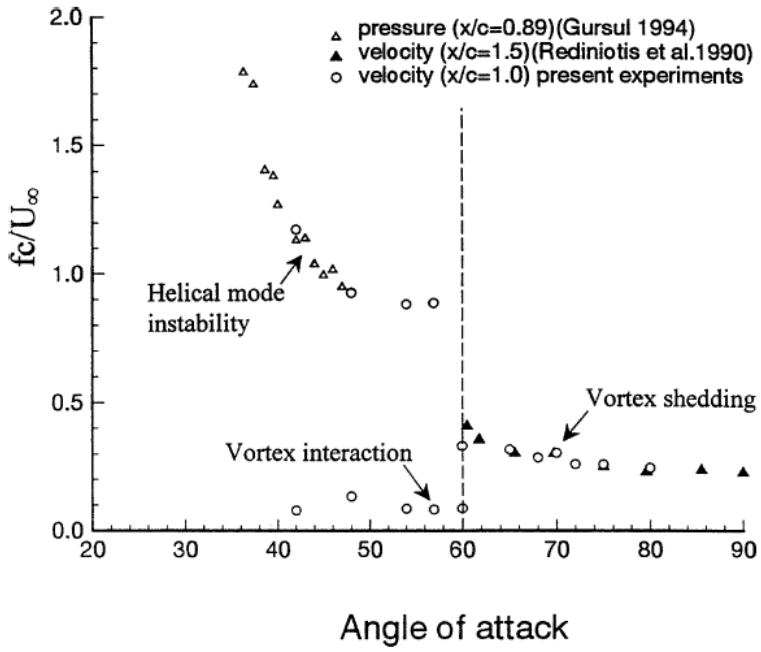

Figure 2.6 Dimensionless frequency variation for unsteady phenomena as a function of AoA [13]

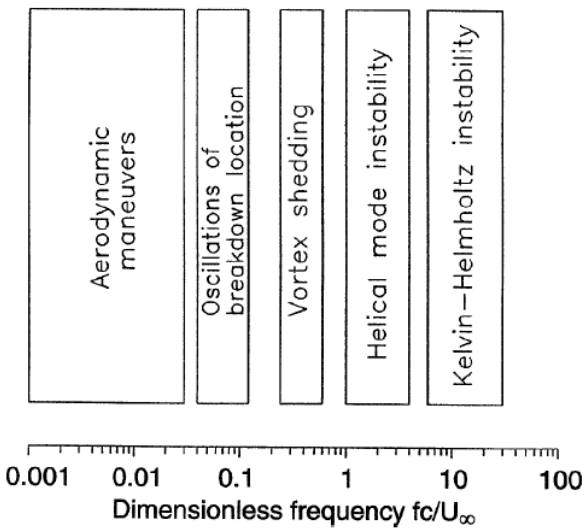

Figure 2.7 The non-dimensional frequency range of unsteady flow phenomena over delta wings [13]

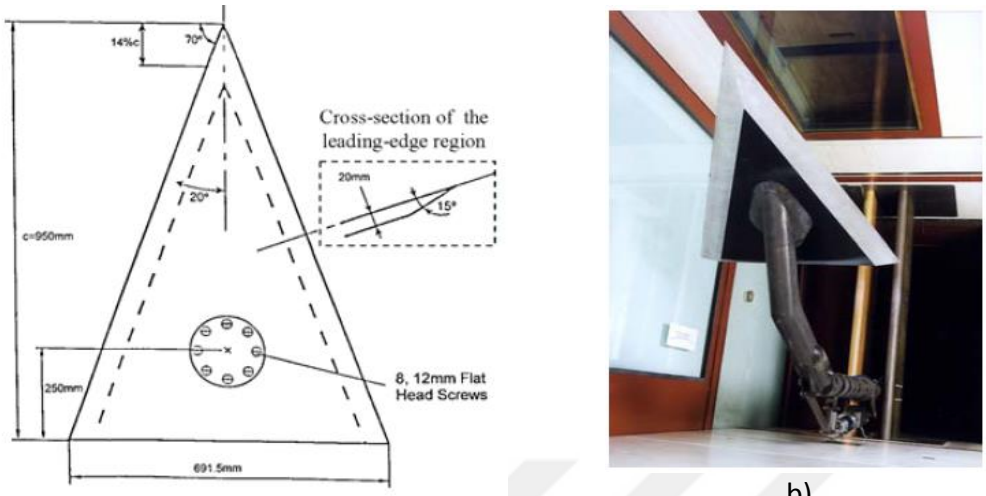

a) b)

Figure 2.8 Delta wing configuration: a) schematic, b) real model in the experiment [20, 21]

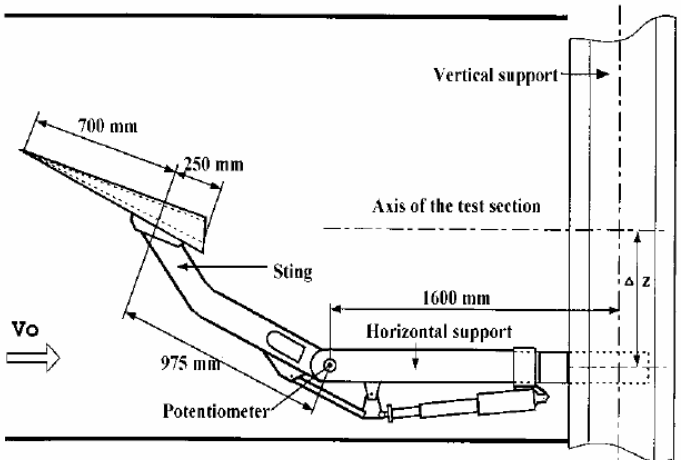

Figure 2.9 Experimental configuration of delta wing in F2 tunnel [21]

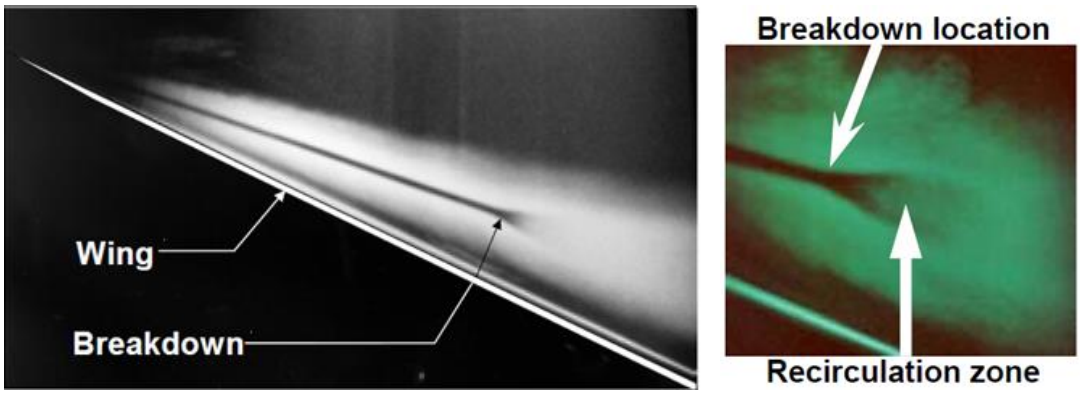

a) b)

Figure 2.10 Instant images of laser sheet: a) side view, b) close view to vortex breakdown location [21]

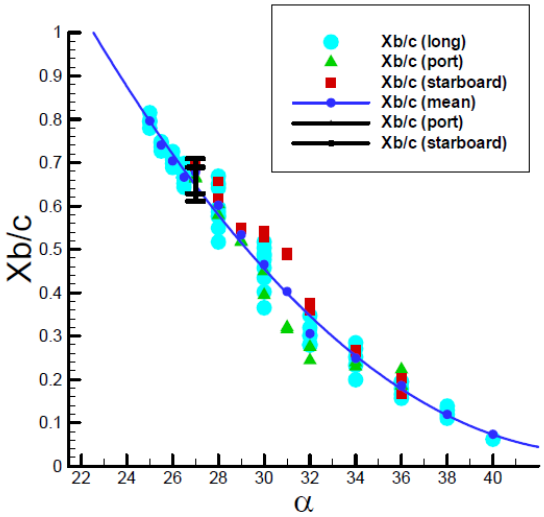

Figure 2.11 Evolution of breakdown location as a function of AoA [21]

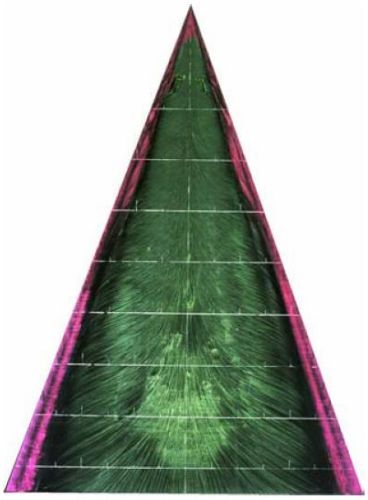

Figure 2.12 Surface oil flow visualization at AoA = 27° and U_∞ = 24 m/s [21]

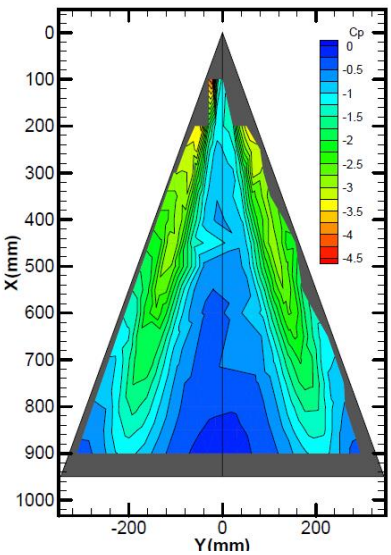

Figure 2.13 Cp contour on the upper surface of the delta wing at AoA = 27° and freestream velocity of 24 m/s [21]

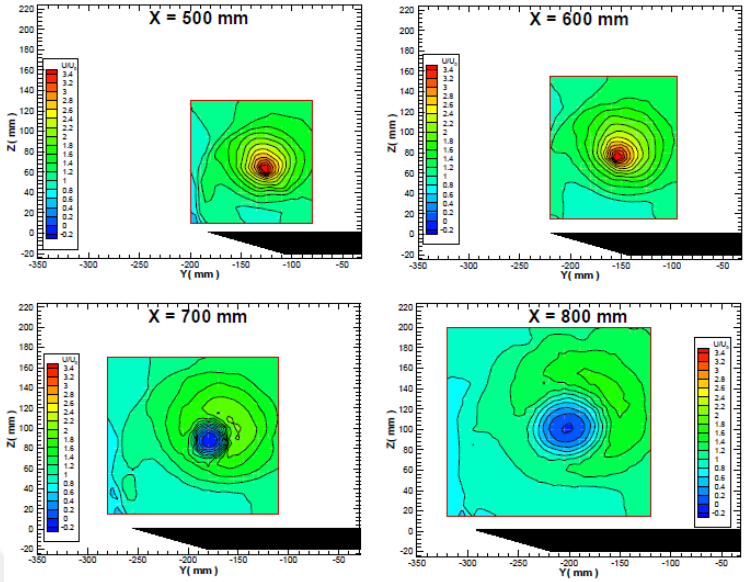

Figure 2.14 Non-dimensional axial velocity at AoA = 27° and U = 24 m/s at four different planes perpendicular to upper surface: X = 500 mm, X = 600 mm, X = 700 mm, X = 800 mm [21]

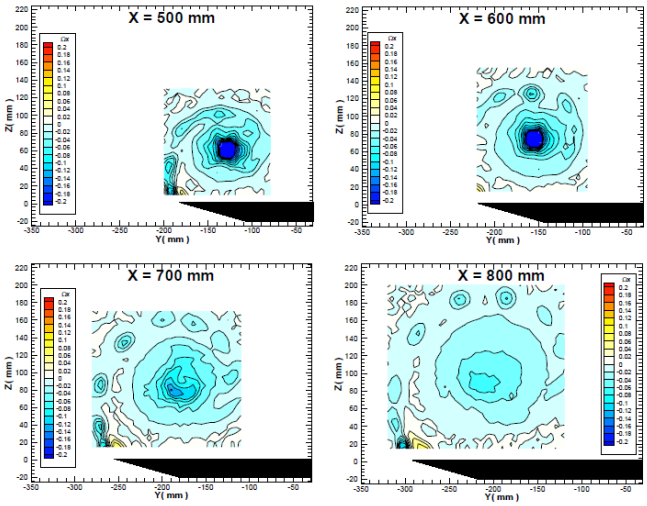

Figure 2.15 Non-dimensional axial vorticity at AoA = 27° and U = 24 m/s at four planes perpendicular to upper surface: X = 500 mm, X = 600 mm, X = 700 mm, X = 800 mm [21]

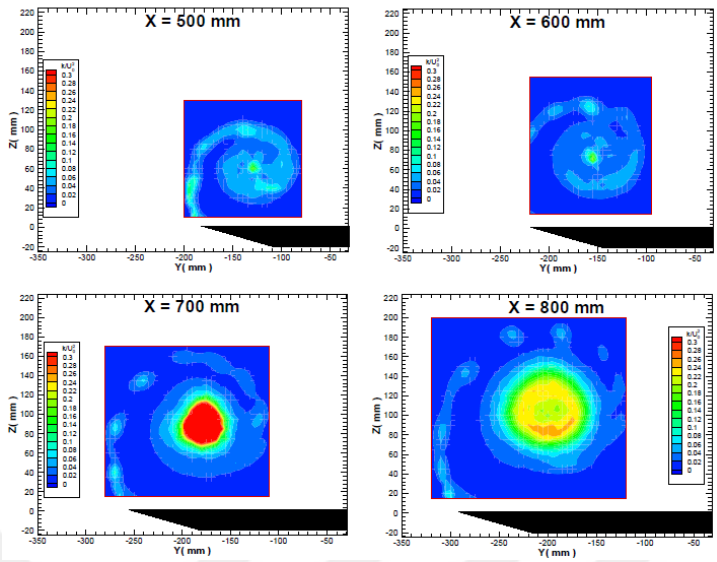

Figure 2.16 Non-dimensional turbulent kinetic energy at AoA = 27° and U = 24 m/s at four planes perpendicular to upper surface: X = 500 mm, X = 600 mm, X = 700 mm, X = 800 mm [21]

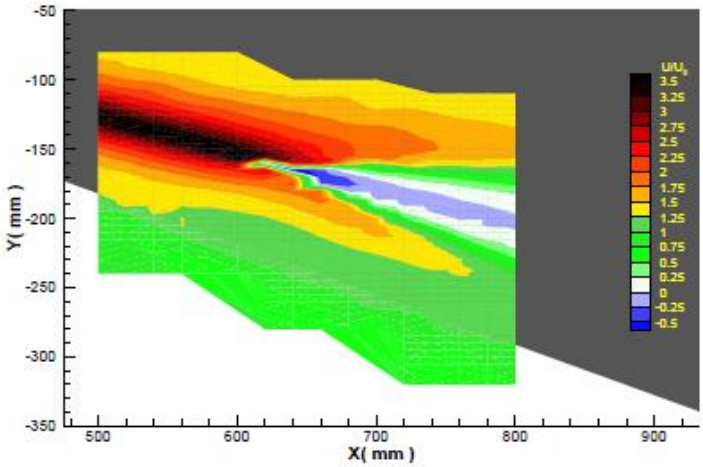

Figure 2.17 Non-dimensional axial velocity contour in the plane which longitudinally intersects vortex core at AoA = 27° and U = 24 m/s [21]

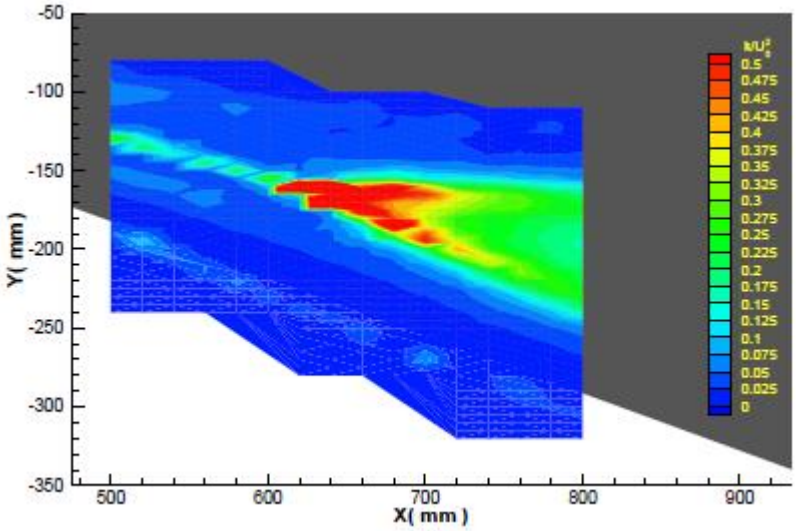

Figure 2.18 Non-dimensional TKE contour in the plane which longitudinally intersects vortex core at AoA = 27° and U = 24 m/s [21]

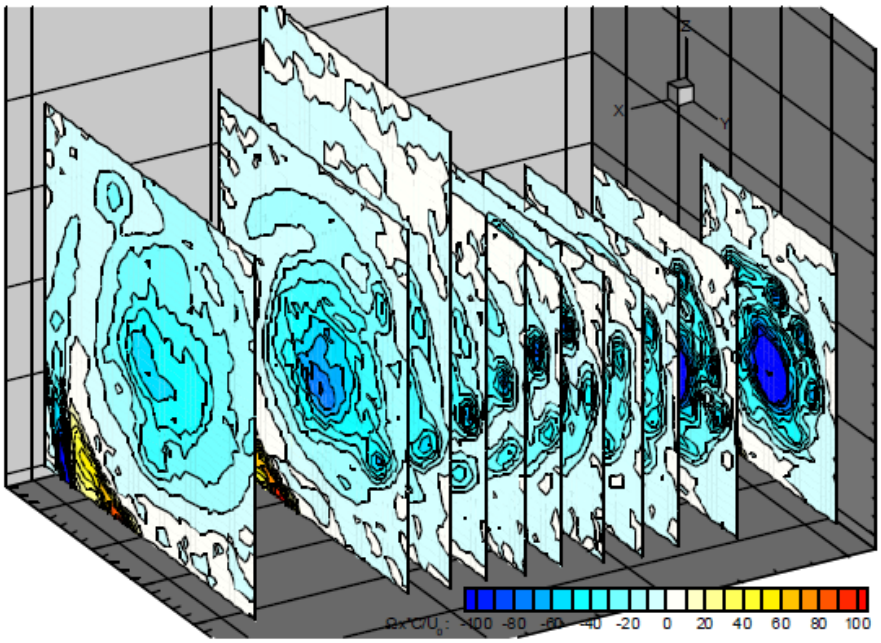

Figure 2.19 LDC results of non-dimensional axial vorticity at 14 different planes perpendicular to the leeward surface of the delta wing [15]

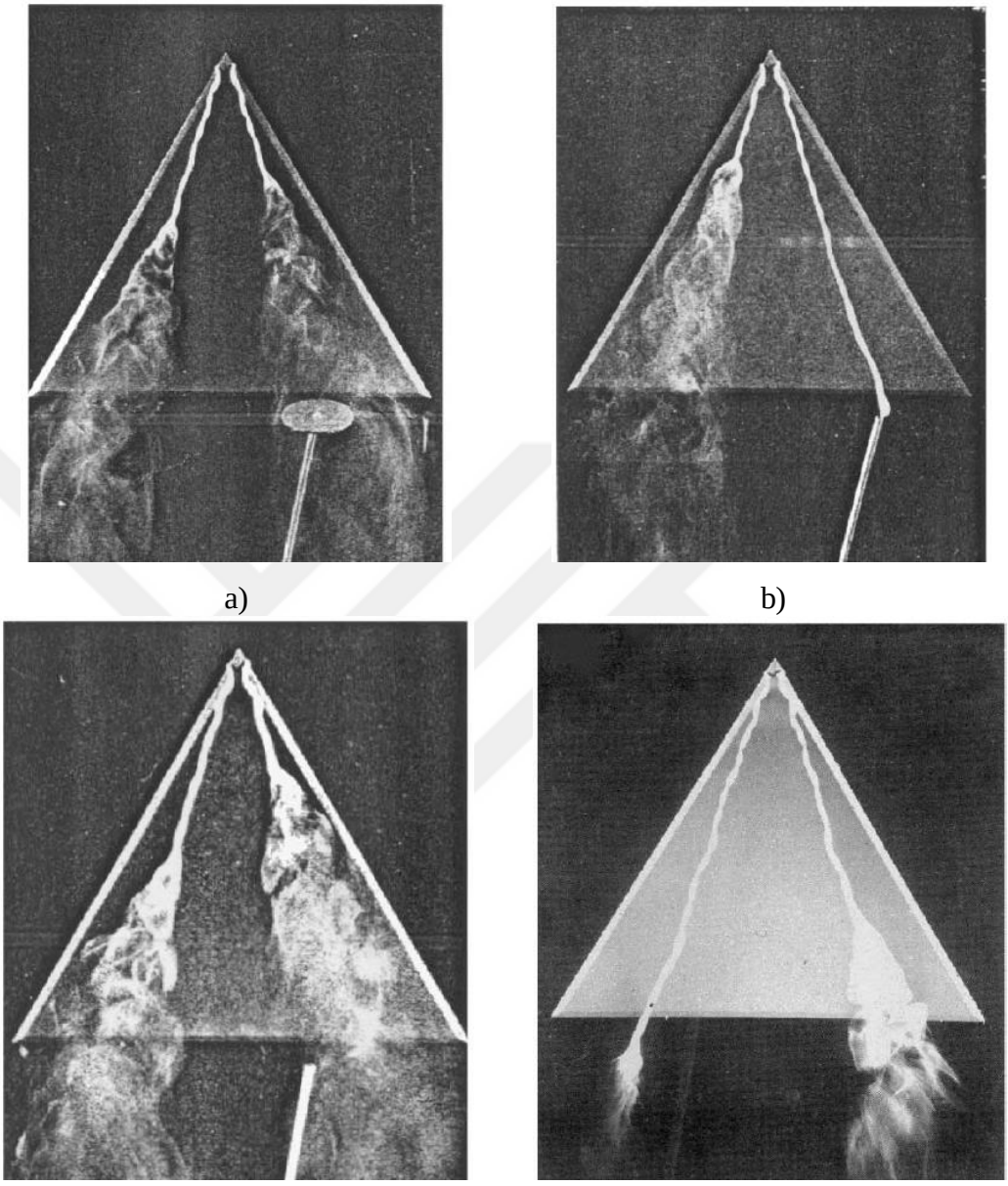

Figure 2.20 Effects of various flow control methods on leading edge vortices of a 60^0 sweep slender delta wing with sharp leading edges at an angle of attack of 20^0: a) Obstacle located downstream, b) Trailing edge suction, c) Flow ejection counter to the axial velocity of the vortex core, and d) Along-the-core blowing to left side of vortex [32]

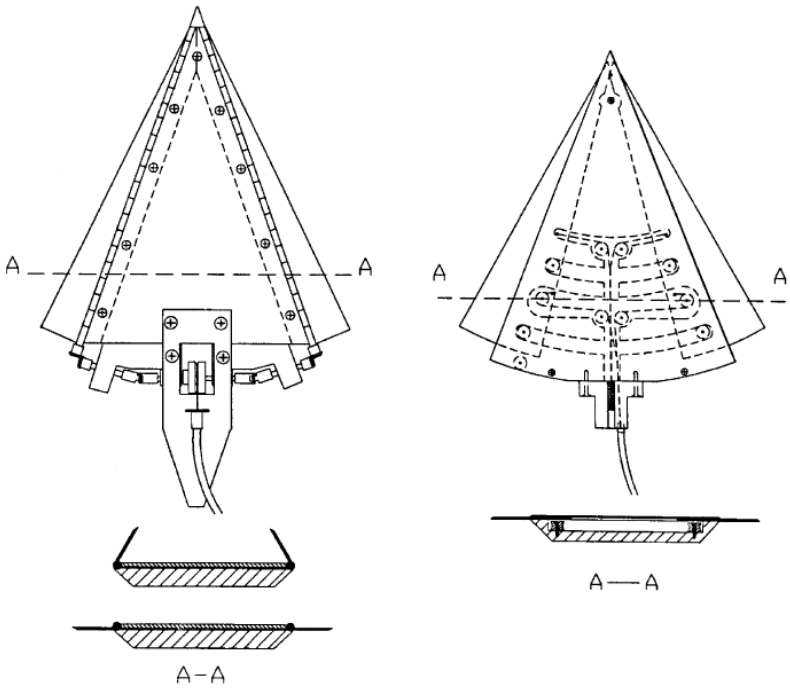

Figure 2.21 Flaps located at leading edge and variable sweep equipment studied by Gursul et al. [32]

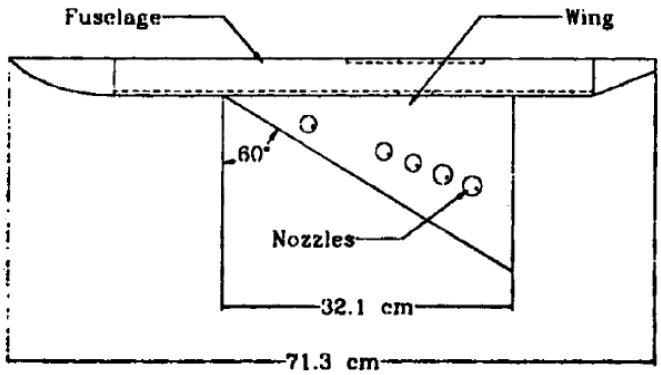

Figure 2.22 Location of five blowing nozzles for along the core blowing [34]

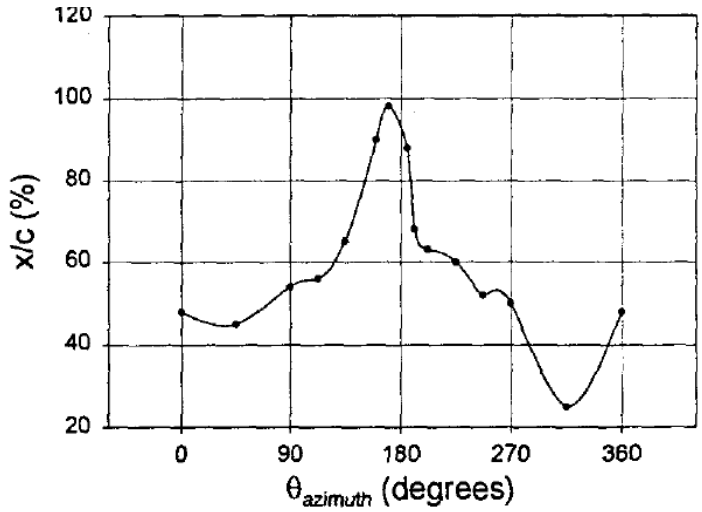

Figure 2.23 Performance of blowing as a function of azimuthal angle with constant blowing coefficient (C_μ = 0.01) [34]

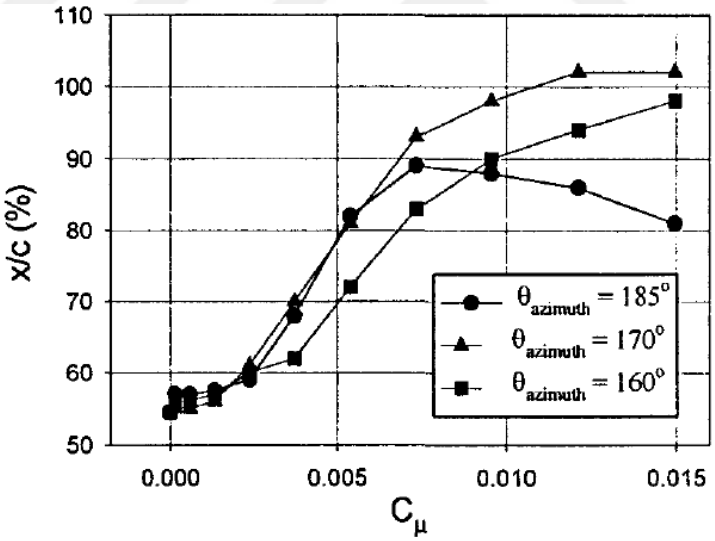

Figure 2.24 Relationship between breakdown location and blowing momentum for three azimuthal angles [34]

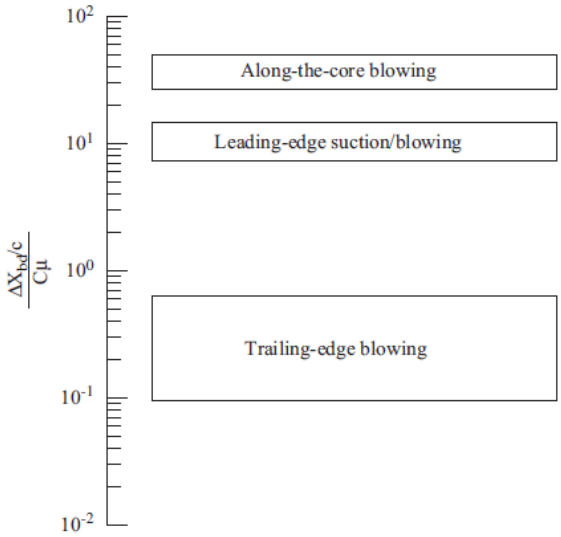

Figure 2.25 Effectiveness of blowing/suction control techniques [47]

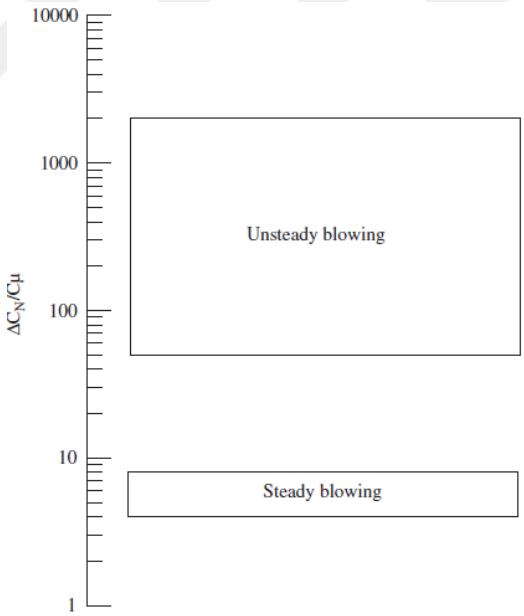

Figure 2.26 Effectiveness comparison of steady and unsteady blowing [47]

CHAPTER 3

SIMULATION MODEL

In this chapter, the CFD model is explained in detail including the solution domain, grid information, and solution parameters. The simulation domain is created in the ANSYS Design Modeler. The unstructured grid is generated by using ANSYS Meshing and then transferred to ANSYS/FLUENT for the steady state simulations utilizing various RANS turbulence models. In the study, the flow is assumed to be incompressible and the energy equation does not need to be solved.

3.1 Simulation Domain, Boundary Conditions, and Simulation Parameters

The dimensions of the delta wing model are identical to those of the experimental study of Mitchell [20, 21] and have a sweep angle (Λ) of 70^0, root chord (c) of 950 mm, and wingspan of 691.5 mm. The thickness of the wing is 20 mm, and it is beveled on the windward side at an angle of 15^0 to form sharp leading-edges. Sting and horizontal support are excluded from the simulation model as shown in Figure 3.1. The dimensions of the simulation model are taken similar to the previously conducted CFD studies summarized in section 2.2.2. Dimensions of the simulation domain in terms of root chord length are tabulated in Table 3.1.

Simulations are focused on the experimental conditions at AoA of 27° and freestream velocity of 24 m/s with corresponding Mach number of 0.0706 and root chord Reynolds number of 1.56×10^6, which is fully consistent with test conditions.

Velocity inlet and pressure outlet boundary conditions are applied for the surfaces labeled as “Inlet” and “Outlet” in Figure 3.1, respectively. Top, bottom, and side

wall of the simulation domain as well as surfaces of the delta wing are modeled as no-slip boundary conditions where velocity of the fluid is zero relative to the boundary. Due to the symmetry of the flow field, a half domain is used in the simulations and the symmetry boundary condition is considered for the plane of symmetry. Details of the boundary conditions are given in Table 3.2.

A SIMPLE scheme is chosen for the pressure-velocity coupling, a Green-Gauss Node Based scheme is selected for the gradient, and a second order scheme for pressure is chosen for spatial discretization. A second order upwind scheme for the momentum, turbulent kinetic energy, and specific dissipation rate are selected to obtain more accurate results than the first order upwind scheme.

3.2 Grid Information, Mesh Independence and Computation Time

A 3D unstructured grid involving tetrahedral and wedge/prism cells is generated with the patch conforming method. The number of elements in the mesh independence study is controlled by the face sizing option, which controls the mesh density of leeward and rearward surfaces of the delta wing. The mesh size of the delta wing edges is set to 1.2 mm with the edge sizing option to capture the primary separation line (leading edge) precisely for all simulations. The y^+ value is kept below 1.1 for all simulations.

Detailed information about the grids used in the mesh independence study is provided in Table 3.3. Four cases having approximately 1, 4, 10, and 15 million elements are considered for the mesh independence study. Figure 3.2 shows the general and sectional view of Mesh 3 that has around 10 million elements.

In the case of the mesh independence study, k-ω SST with low-Re correction and the curvature correction turbulence model is used. In the simulations, residuals of Mesh 3 shown in Figure 3.3 and pressure coefficient (Cp) at four chordwise line stations of Mesh 3 (X = 500 mm, X = 600 mm, X = 700 mm, and X = 800 mm as

shown in Figure 3.4) are tracked to check convergence. Figure 3.5 shows the X = 800 mm chordwise station of Mesh 3 case at different iterations. In that case, pressure coefficient value is decreased and converged to the certain value as the iterations proceed. The performed simulations are converged between 1500 to 3000 iterations case by case.

The vortex breakdown location and pressure coefficient (Cp) are the two parameters used to check mesh independency. In this study, vortex breakdown location is defined as the position where streamwise velocity goes to zero in the vortex core. This approach was previously used in the studies of Allan [1], Soemarwoto [26], Görtz [28], and Morton [31]. Table 3.4 shows the vortex breakdown location for four cases. It is seen that as the mesh becomes finer, the vortex breakdown location moves to the apex direction and converges to 66 % of the root chord. As previously mentioned in the literature review section, negative azimuthal vorticity slows down the axial velocity and eventually yields to stagnation and recirculation, according to Lopez et al. [8, 9 and 12]. For that purpose, azimuthal vorticity contours in the plane which intersects the vortex core longitudinally for 4 mesh cases are presented in Figure 3.6 in order to observe the sign change of azimuthal vorticity, which is a good indication of vortex breakdown.

The second parameter to check mesh independency is the pressure coefficient (Cp), which is plotted at four chordwise line stations (X = 500 mm, X = 600 mm, X = 700 mm, and X = 800 mm) for four cases as shown in Figure 3.7. It is seen that the Cp results of Mesh 3 and Mesh 4 demonstrate similar behavior and that their peak magnitudes at four chordwise stations do not vary more than 2 %. Since Mesh 3 contains fewer elements when compared with Mesh 4, Mesh 3 is the selected case for further studies in the thesis. It is important to note that one can consider the Cp values of Mesh 2 to also be closer to Mesh 3 and Mesh 4, but the vortex breakdown location is the most determinative criterion for the mesh independence study.

The computation time of Mesh 1, Mesh 2, Mesh 3 and Mesh 4 for 2500 iterations are summarized in Table 3.5 for comparison. Eight-Core-Processor of 3.5 GHz AMD FX™-8320 is used for performing the numerical computations.

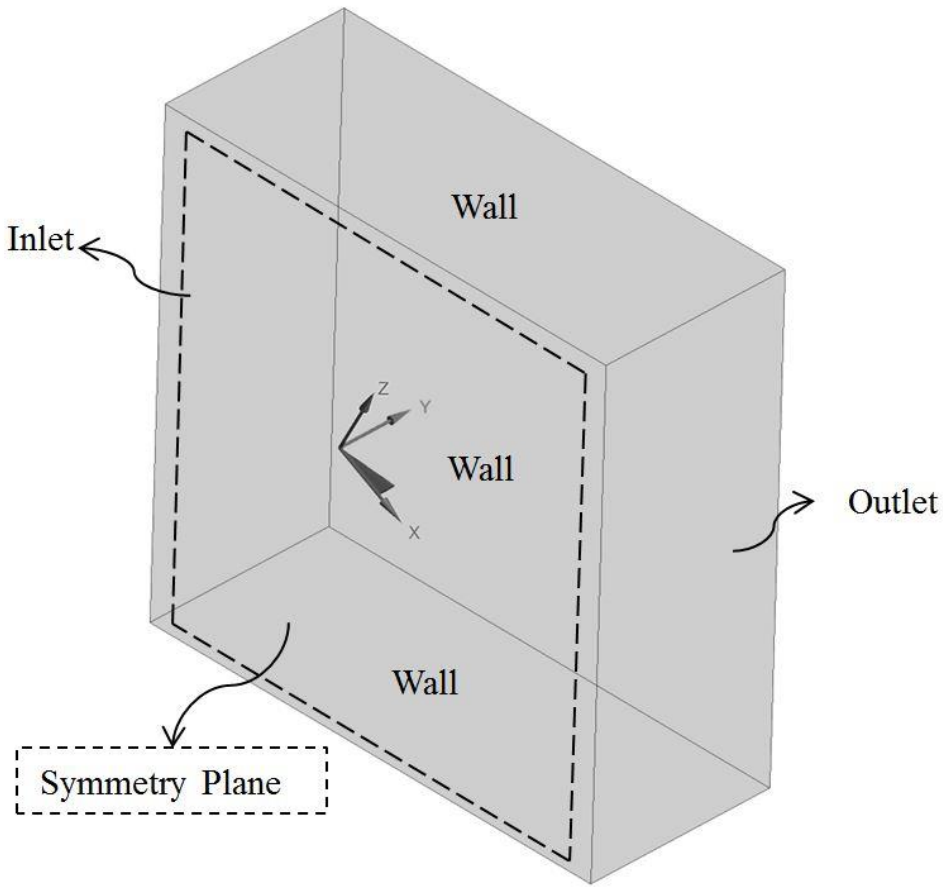

Figure 3.1 Simulation domain

Table 3.1 Dimensions of the simulation domain in terms of root chord

Simulation Domain	**Dimension (RC)**
Up From Wing Apex	4.5
Down From Wing Apex	5.5
Upstream From Apex	4.1
Downstream From Apex	5.9
Spanwise From Wing Centerline	4.0

Table 3.2 Details of the boundary conditions

Surface Name	**Boundary Type**	**Parameter**	**Value**
Inlet	Velocity Inlet	Velocity (m/s)	24
		Turbulent Intensity (%)	0.1
		Turbulent Viscosity Ratio	10
Outlet	Pressure Outlet	Gauge Pressure (Pa)	0
Wall	Wall	No Slip	-
Symmetry Plane	Symmetry	-	-

Table 3.3 Details of grids used in mesh independency study

	Mesh 1	**Mesh 2**	**Mesh 3**	**Mesh 4**
Number of Nodes	225,155	1,104,521	3,147,504	4,984,586
Number of Elements	997,968	4,010,853	10,052,886	15,399,415
Maximum Skewness	0.97	0.97	0.97	0.97
Average Skewness	0.23	0.21	0.20	0.20
Maximum Aspect Ratio	6,436.60	2239.30	1,358.10	649.86
Average Aspect Ratio	48.77	35.00	26.18	21.78

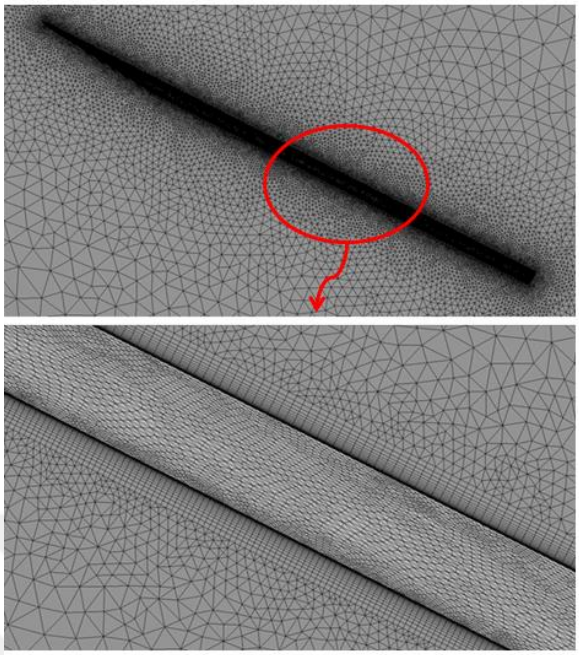

a)

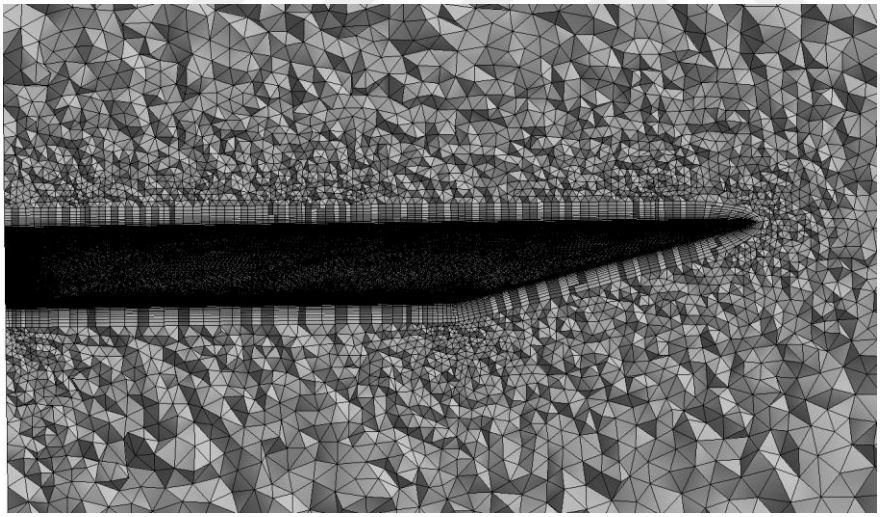

b)

Figure 3.2 Mesh 3: a) General view, and b) Sectional view

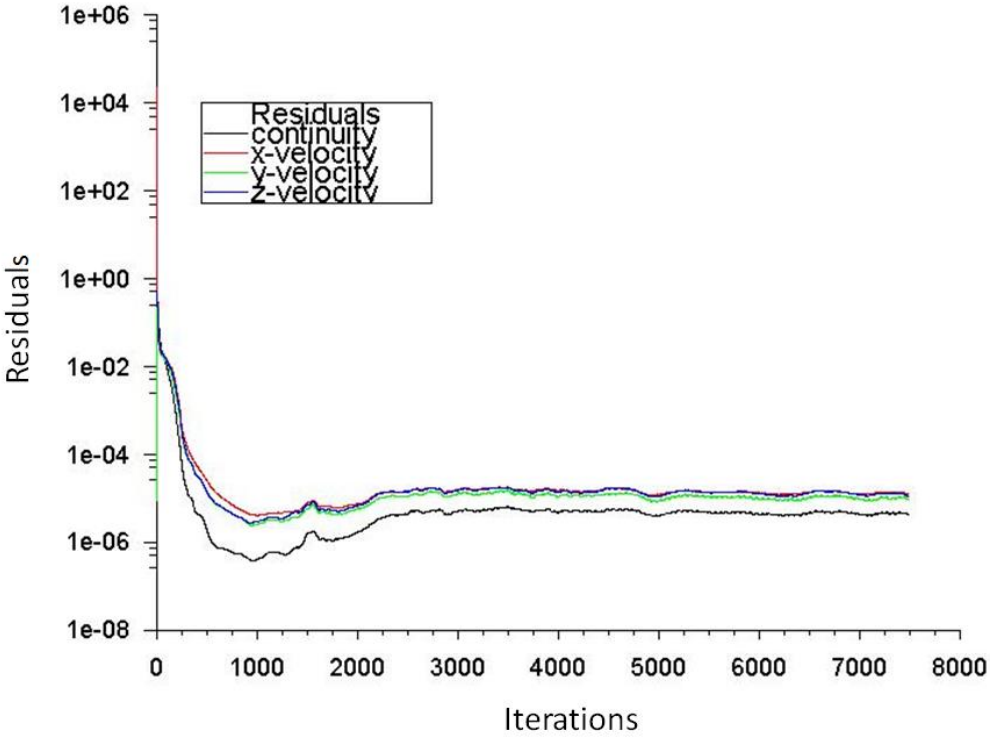

Figure 3.3 Convergence history of the simulation

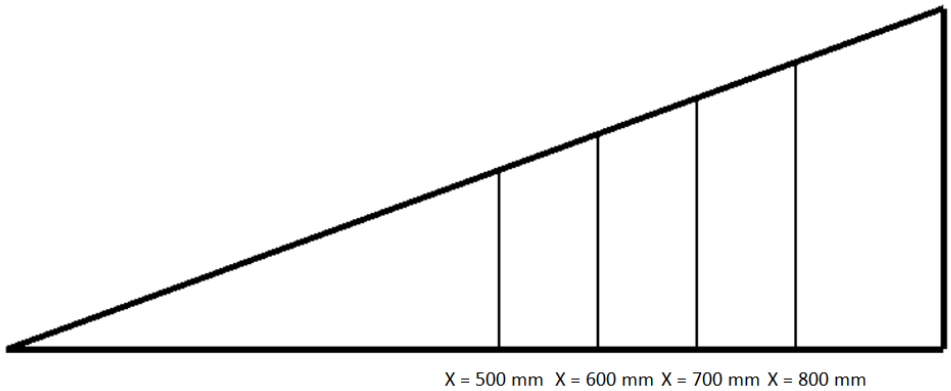

Figure 3.4 Four chordwise line stations (X = 500 mm, X = 600 mm, X = 700 mm, and X = 800 mm)

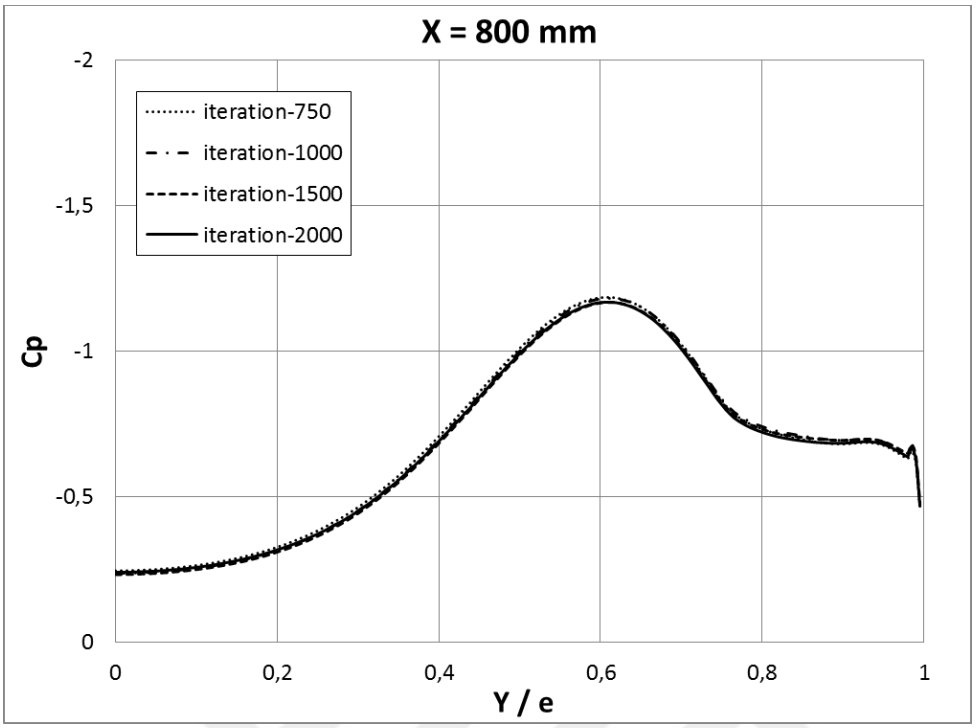

Figure 3.5 Pressure coefficient (Cp) – iteration chart of Mesh 3

Table 3.4 Vortex breakdown locations of four cases

	Vortex Breakdown Location (Xb / c)
Mesh 1	0.84
Mesh 2	0.70
Mesh 3	0.66
Mesh 4	0.66

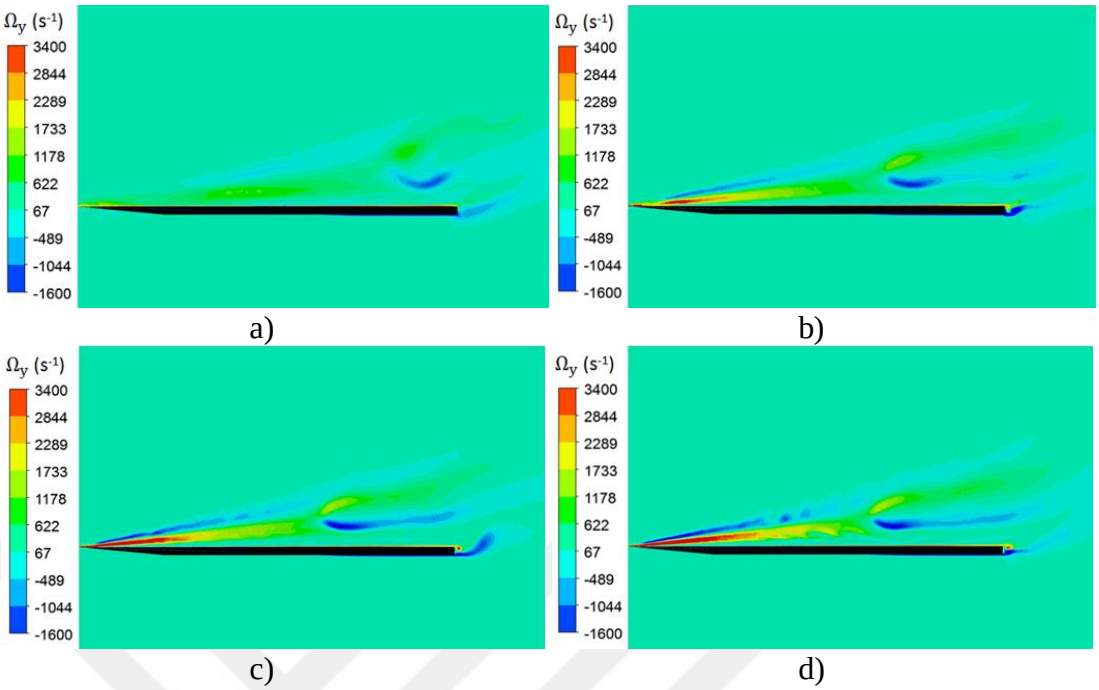

Figure 3.6 Azimuthal vorticity contour of a) Mesh 1, b) Mesh 2, c) Mesh 3, and d) Mesh 4

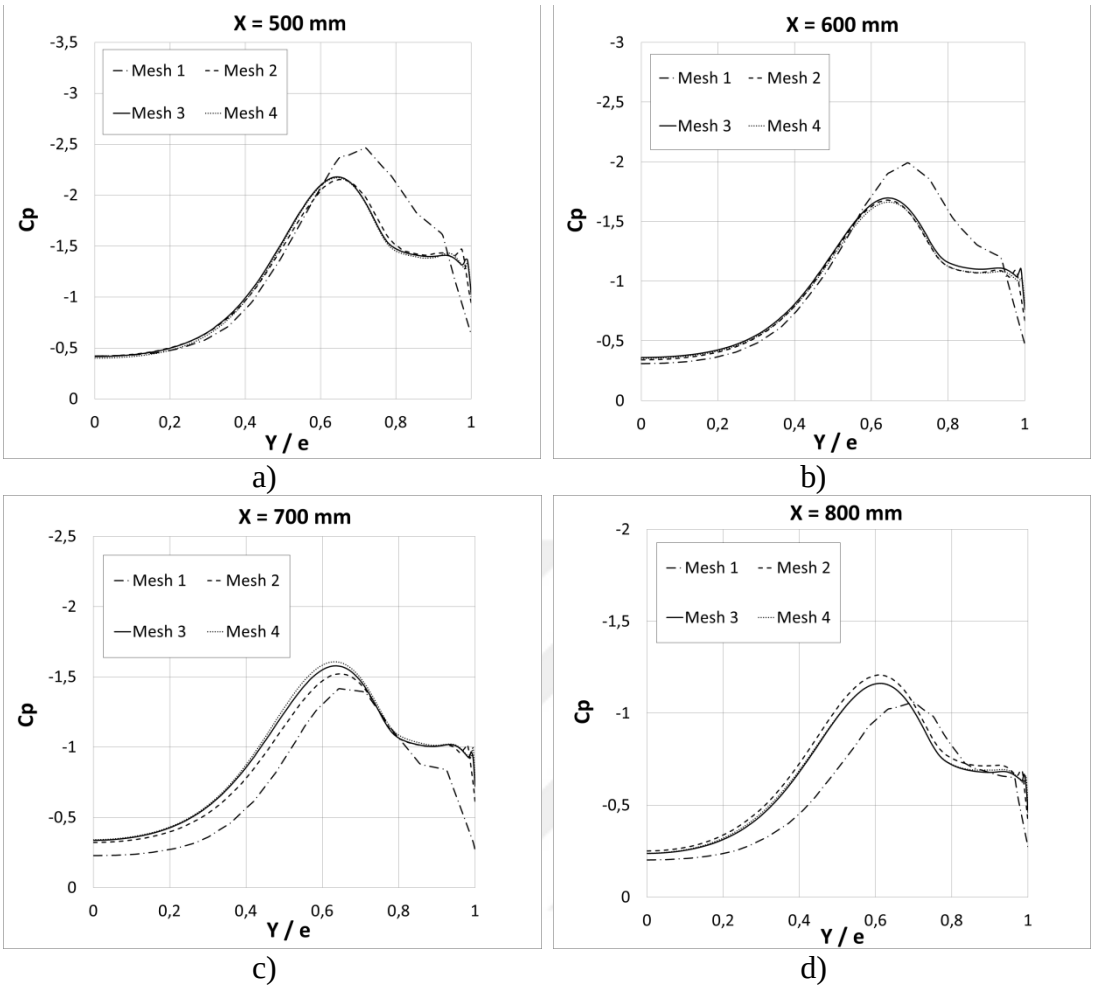

Figure 3.7 Pressure coefficients of four cases at four different chordwise locations: a) X = 500 mm, b) X = 600 mm, c) X = 700 mm, and d) X = 800 mm

Table 3.5 The computation time of four mesh cases

	Iteration	**Total wall-clock time (h)**
Mesh 1	2500	1.9
Mesh 2		10.6
Mesh 3		34.0
Mesh 4		55.4

CHAPTER 4

COMPARISON AND VERIFICATION OF TURBULENCE MODELS

In this chapter, different turbulence models with additional corrections are presented and compared with experimental results along with the previously conducted numerical studies. In this chapter, Mesh 3 is the case used for the comparison and verification of the turbulence models.

The investigated turbulence models and the associated corrections are presented in Table 4.1. This table also shows the vortex breakdown locations of the investigated turbulence models and the corrections. It is demonstrated that the curvature correction (CC) option promotes the vortex breakdown location for both k-ω SST and Spalart-Allmaras turbulence models. Vortex breakdown locations of k-ω SST LRC-CC and k-ω SST CC are the same and equal to 66 % of the root chord, which is the closest value to the time-averaged vortex breakdown location (65 %) of Mitchell's experimental study [20, 21]. To clearly visualize the location of breakdown, the azimuthal vorticity contour passing through the vortex core is shown in Figure 4.1.

Figure 4.2 demonstrates the pressure coefficients (Cp) along the four chordwise locations. A suction peak of the primary vortex is evident for all turbulence models; however, their pressure levels are underestimated when compared against experimental data. A small suction peak near the primary separation line (leading edge) is the indication of secondary vortices that cannot be identified from the Cp results of the experiment due to the resolution of the experimental study.

At different locations, different turbulence models show higher suction peak and correspond to the experimental result. When the Cp results of the k-ω SST LRC-CC and k-ω SST CC turbulence models are compared, it is seen that k-ω SST CC

gives a slightly higher suction peak. Therefore, k-ω SST with CC is the selected turbulence model that will be used in further comparison with experimental data and previously conducted numerical studies.

The pressure coefficient of the current study is compared with previous numerical studies that are summarized in Section 2.2.2 and with experimental results at four different chordwise locations in Figure 4.3. It is seen that all studies underestimate the peak value and that there is not a single model that reaches the highest peak at all chordwise locations. According to Morton [31], possible source of the underestimation of Cp between all of the computational simulations and the experimental results could be because of a difference in the reference dynamic pressure scaling. Table 4.2 presents the vortex breakdown location of the experiment, current study, and the previous numerical studies. Very close agreement between the current study and experiment is observed.

As previously mentioned in Section 2.2.1, suction peak is placed at roughly 66% of the wingspan (Y / e) in the experiment. Table 4.3 presents the calculated higher suction peaks at three different downstream positions (X = 300 mm, X = 500 mm, and X = 600 mm) of the current study. Quantitative agreement between experimental data and the current study is observed.

In order to calculate the angle between the vortex core and the upper surface of the delta wing, the highest non-dimensional axial vorticity points at three downstream positions (X = 300 mm, X = 500 mm, and X = 600 mm) are firstly identified. The angle is calculated by using the coordinates of these points. Experimental results and the calculated values are presented in Table 4.4. The calculated angle is slightly underestimated when compared with experimental data, which is 7°.

Projection of these highest non-dimensional axial vorticity points onto the leeward surface is used to calculate the sweep angle of the vortex core, which follows a path from apex to trailing edge. In other words, the x and y coordinates of these highest non-dimensional axial vorticity points are utilized to find the vortex sweep

angle. The experimental value of the sweep angle of the vortex core is 77°, which is slightly higher than the calculated values, as shown in Table 4.5.

Figure 4.4 illustrates the computed and the experimental Cp contour of the upper side of the delta wing. Although the computed Cp results underestimate the suction peak, qualitative agreement with the test is evident. In addition, the computed Cp contour captures the clue of the secondary vortex placed close to the primary separation line, which the test could not capture.

Figure 4.5 shows the comparison of computed and experimental values of the non-dimensional axial velocity (U / U_0) contour at four different planes perpendicular to the top surface. Jet-like flow in the vortex core prior to vortex breakdown is observed for both experimental and computed contours. The value U / U_0 is around 3.5 prior to the vortex breakdown in the experiment. However, the computed peak jet-like flow (U / U_0) is around 2.6. In addition, the magnitude of the computed reversed flow at plane X = 800 is smaller when compared with experimental data. Moreover, numerical simulation yields less sharp results, which means that prior to vortex breakdown, a velocity decrease from the plane X = 500 mm to X = 600 mm is observed in the current study. For the experiment, a jet-like velocity profile is conserved prior to vortex breakdown, then sharp and sudden velocity decrease is observed.

Figure 4.6 shows the comparison of computed and experimental contours of the non-dimensional axial vorticity ($\Omega_x c / U_0$) at four planes perpendicular to the leeward surface of the delta wing. In the shear layer, small vorticity pockets that separate from the primary separation line (leading edge of the delta wing) and join into the vortex core are not observed in the computed results unlike the experimental contours. However, these pockets of eddies are captured as continuous contours. Secondary vortex with opposite sign of vorticity is seen in both computed and experimental results. Similar to the U / U_0 contours, the magnitude of computed non-dimensional axial vorticity is underestimated and simulation produces less sharp results when compared with experimental results.

Dissipation of vorticity in the planes X = 700 mm and X = 800 mm is identified, and this situation verifies that the vortex breakdown has occurred upstream of these planes. In the simulation, the sign of the primary vortex is opposite of the experimental results because of showing a different side (port side and starboard side) of the wing.

Figure 4.7 presents non-dimensional turbulent kinetic energy ($k / (U_0)^2$) contours of both experimental and computed results at four perpendicular planes to the upper side of the delta wing. In the experiment, it is seen that longitudinal oscillation in the vortex breakdown location naturally increases the fluctuations in the flow field, and this causes an increase in the turbulent kinetic energy level at X = 700 mm. Fluctuation of breakdown location of the vortex does not influence the turbulence level at X = 800 mm, and the reason for high turbulence level in that plane is because of the highly disorganized flow field after breakdown [19 - 21]. Computed results also capture that situation of underestimating the magnitude.

Table 4.1 Vortex breakdown location of turbulence models

No.	**Turbulence Model**	**Model Correction**	**Vortex Breakdown Location (Xb/c)**
1	k-ω	Low-Re Corrections (LRC) Shear Flow Corrections Curvature Correction (CC)	No detection
2	k-ω SST	-	0.83
3	k-ω SST	LRC	0.79
4	k-ω SST	CC	0.66
5	k-ω SST	LRC CC	0.66
6	Spalart-Allmaras	-	No detection
7	Spalart-Allmaras	CC	0.60

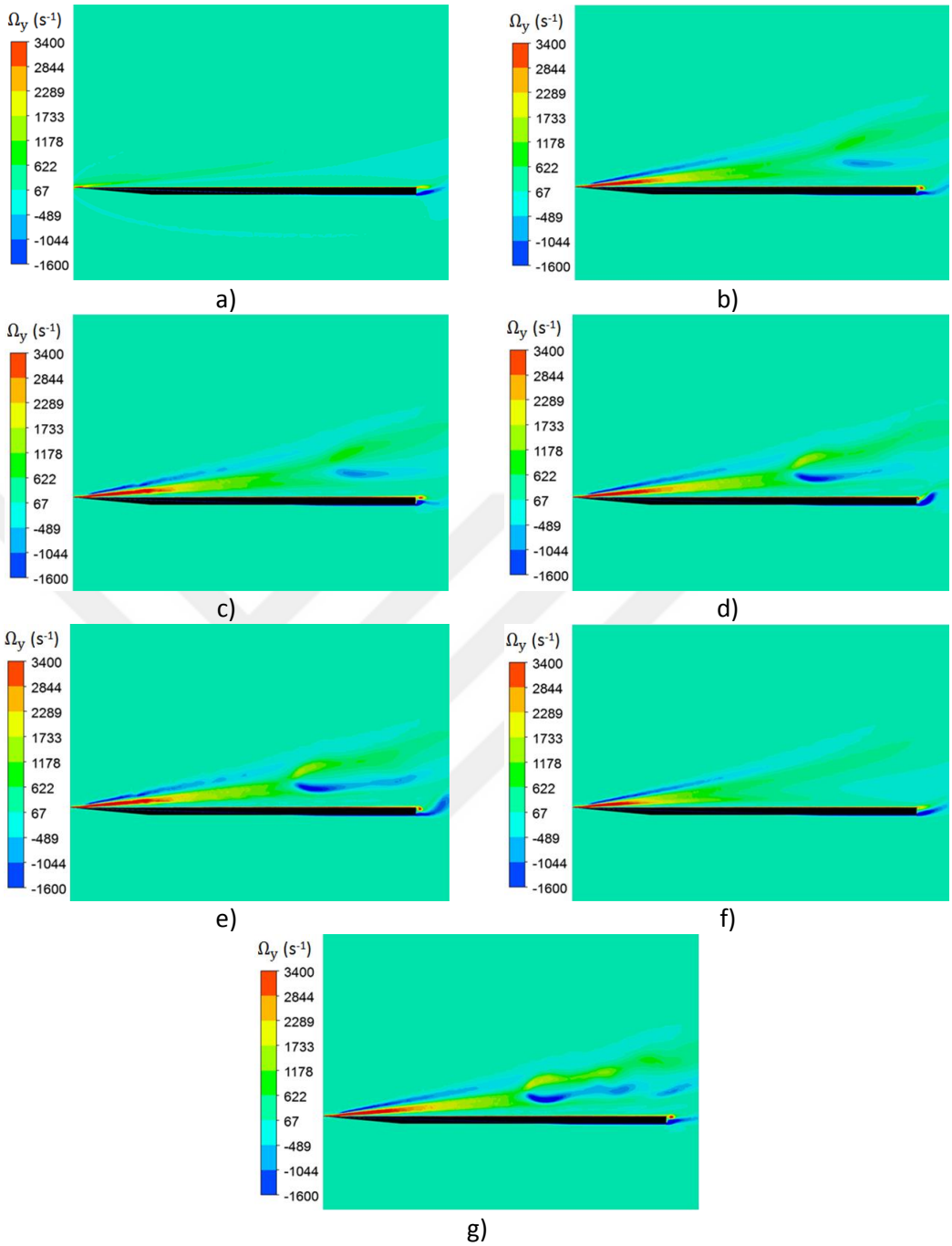

Figure 4.1 Azimuthal vorticity contour passing through vortex core: a) k-ω LRC SFC CC, b) k-ω SST, c) k-ω SST LRC, d) k-ω SST CC, e) k-ω SST LRC CC, f) SA, and g) SA CC

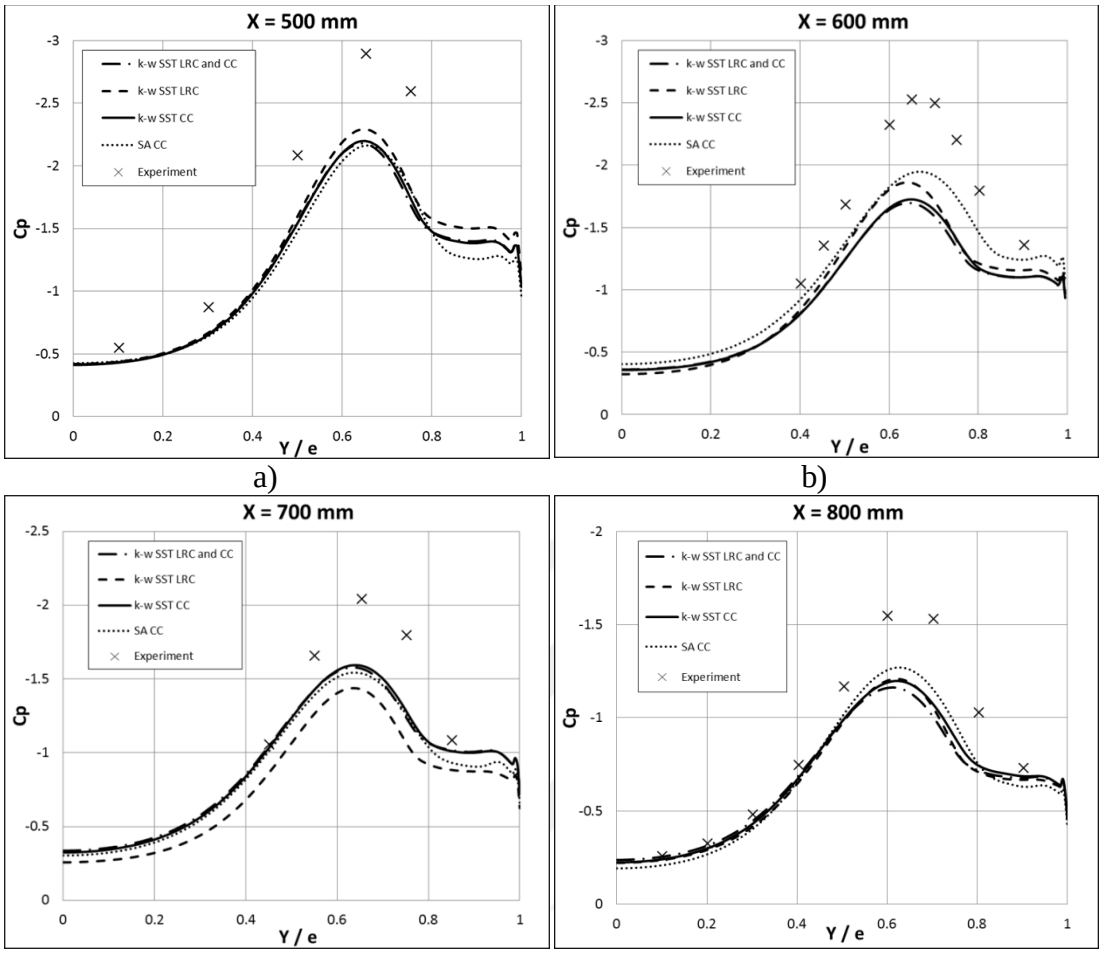

a) b)

c) d)

Figure 4.2 Pressure coefficients of four cases at four different chordwise locations:

a) X = 500 mm, b) X = 600 mm, c) X = 700 mm, and d) X = 800 mm

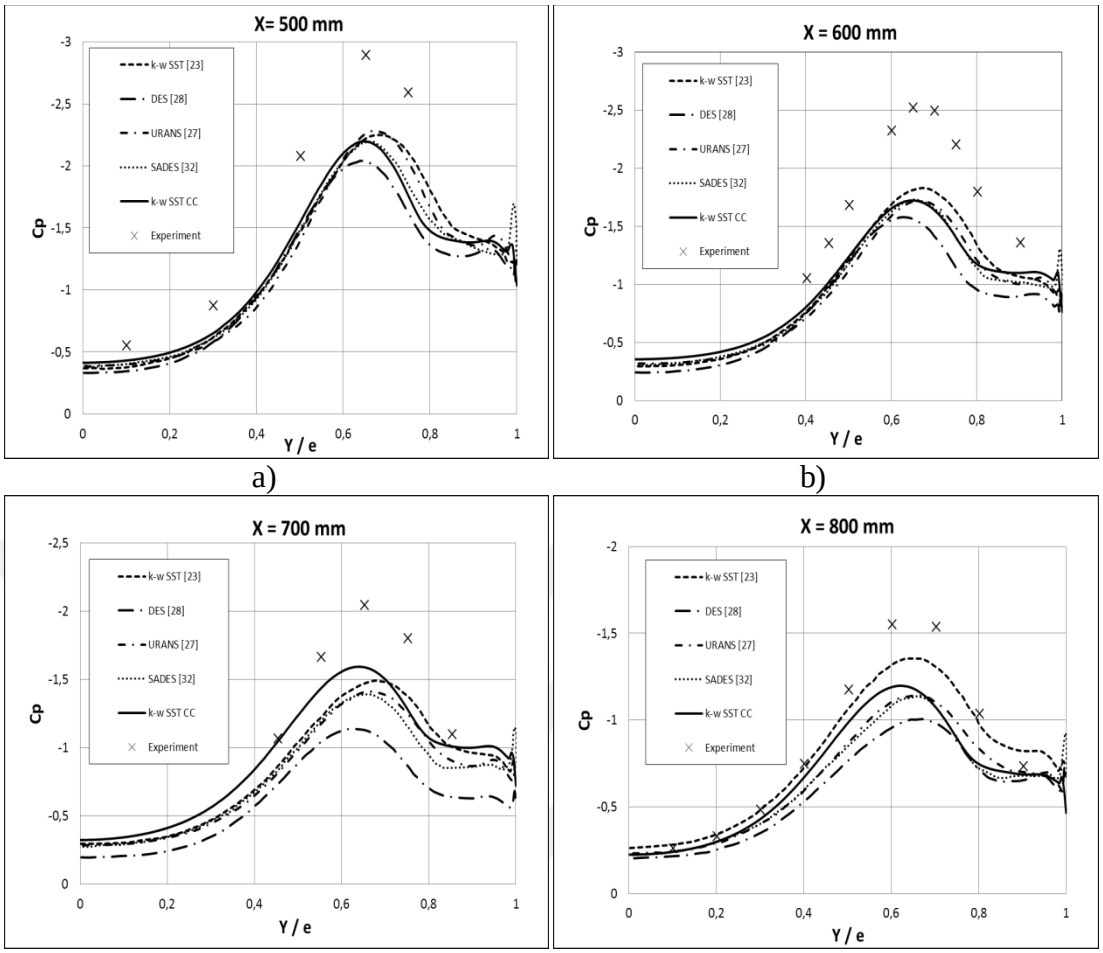

Figure 4.3 Pressure coefficient comparison of previous numerical studies at four different chordwise locations: a) X = 500 mm, b) X = 600 mm, c) X = 700 mm, and d) X = 800 mm

Table 4.2 Vortex breakdown location of previous numerical studies

Study	**Xb /c**
k-ω SST of [23]	0.75
DES of [28]	for the port side 0.789 < Xb/c < 0.813 for the starboard side 0.769 < Xb/c < 0.797
URANS of [27]	0.74
SADES [32]	0.63±0.2
k-ω SST CC	0.66
Experiment (time averaged) [21]	0.65

Table 4.3 Suction peak at three different chordwise locations

X (mm)	**Suction Peak (Y / e)**
300	0.66
500	0.65
600	0.65
Experiment [21]	0.66

Table 4.4 Angle between the vortex core and the leeward surface at three different chordwise locations

X (mm)	**Angle between the vortex core and the leeward surface (°)**
300	6.6
500	6.3
600	6.1
Experiment [21]	7

Table 4.5 Vortex sweep angle at three different chordwise locations

X (mm)	Vortex Sweep Angle (°)
300	76.1
500	76.1
600	75.9
Experiment [21]	77

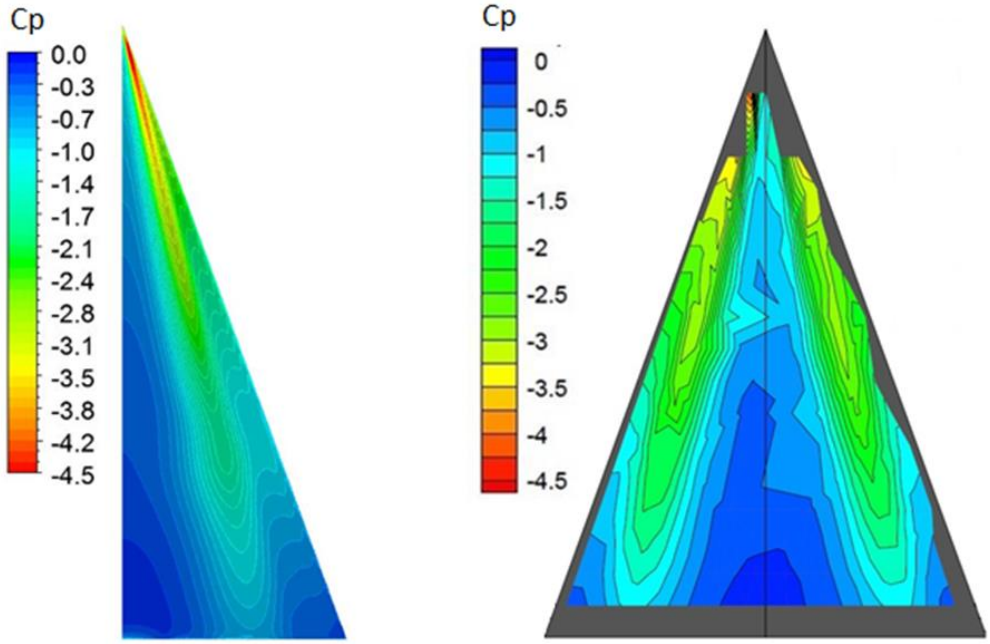

Figure 4.4 Computed (left) and measured [21] (right) pressure distribution of the leeward surface

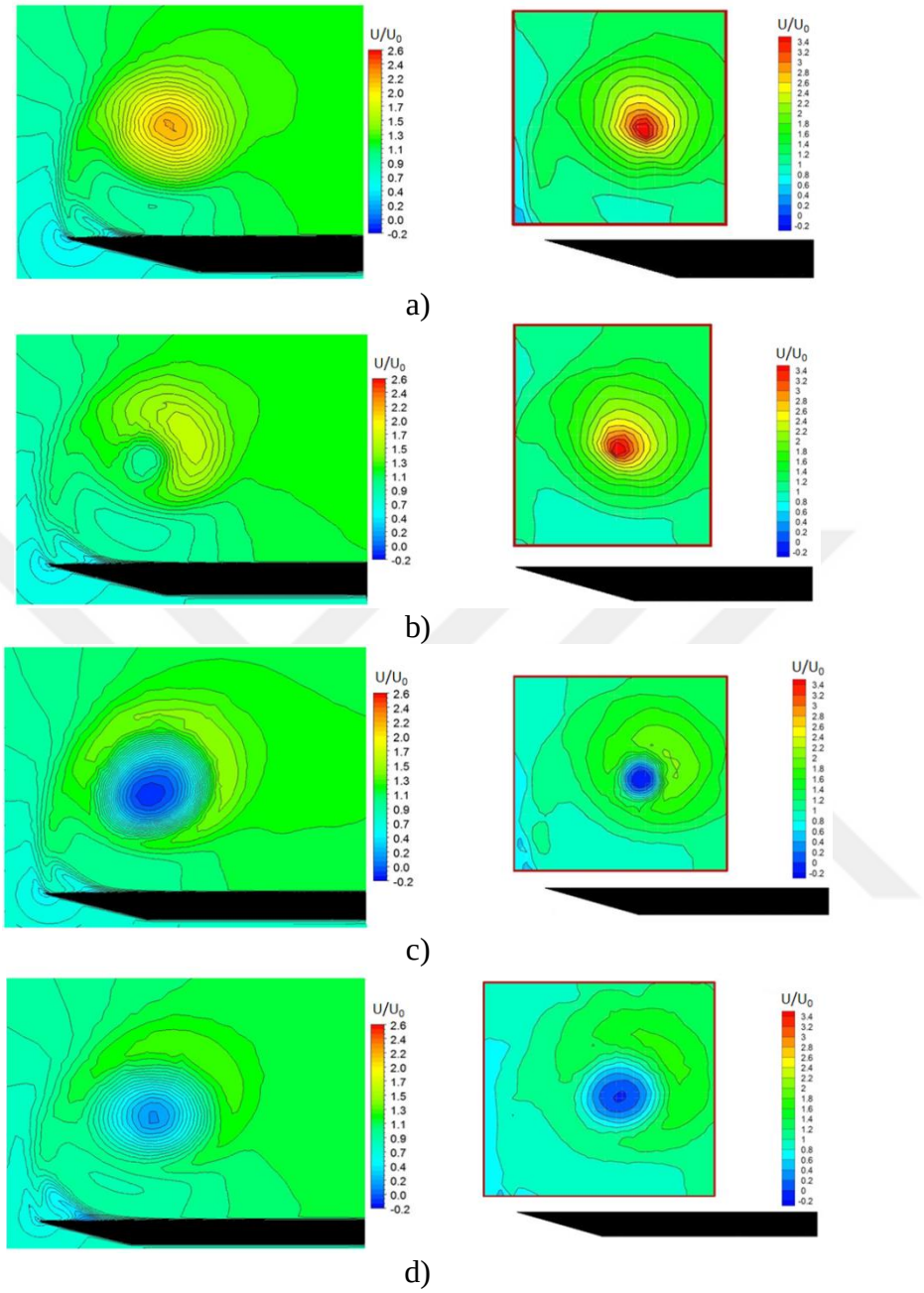

Figure 4.5 Computed (left) and measured [21] (right) non-dimensional axial velocity (U / U_0) at four planes perpendicular to the leeward surface of the delta wing: a) X = 500 mm, b) X = 600 mm, c) X = 700 mm, and d) X = 800 mm

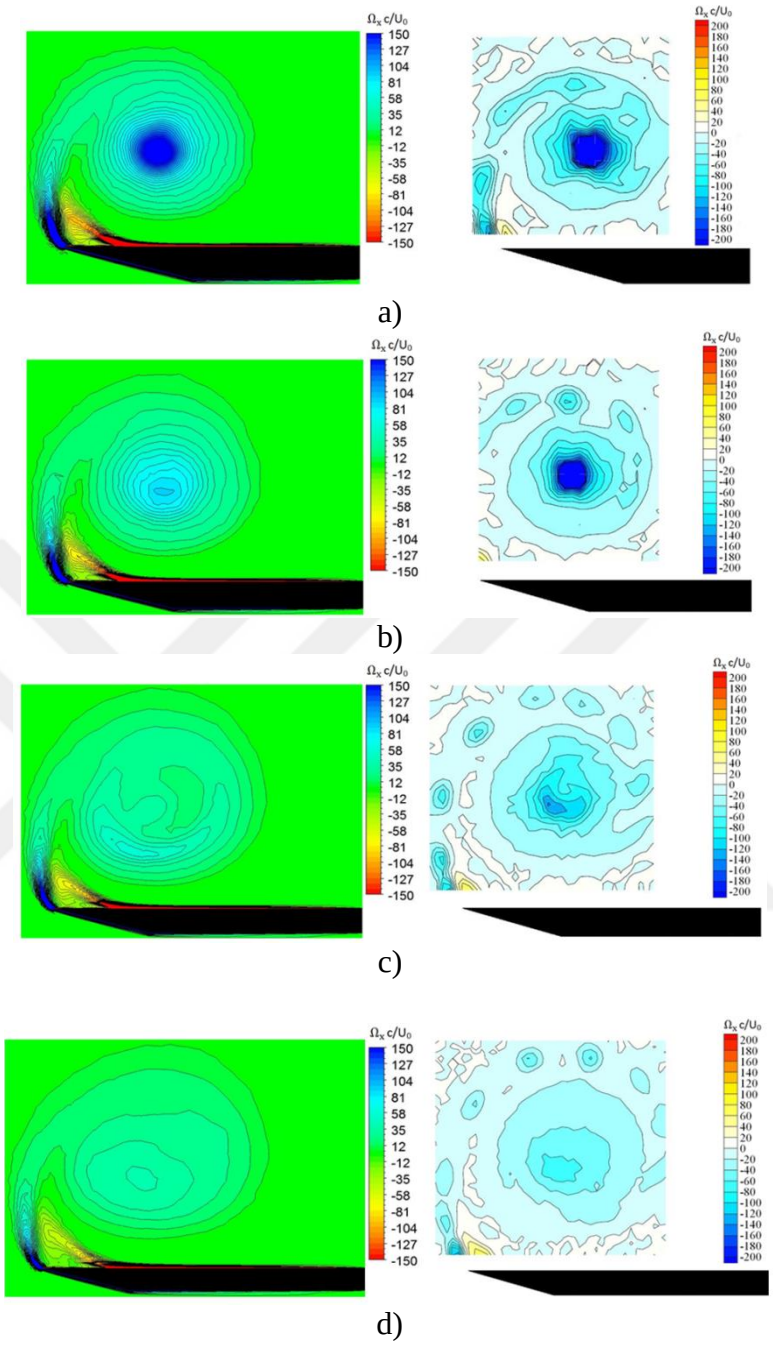

Figure 4.6 Computed (left) and measured [21] (right) non-dimensional axial vorticity (Ω_x c / U_0) at four planes perpendicular to leeward surface of the delta wing: a) X = 500 mm, b) X = 600 mm, c) X = 700 mm, and d) X = 800 mm

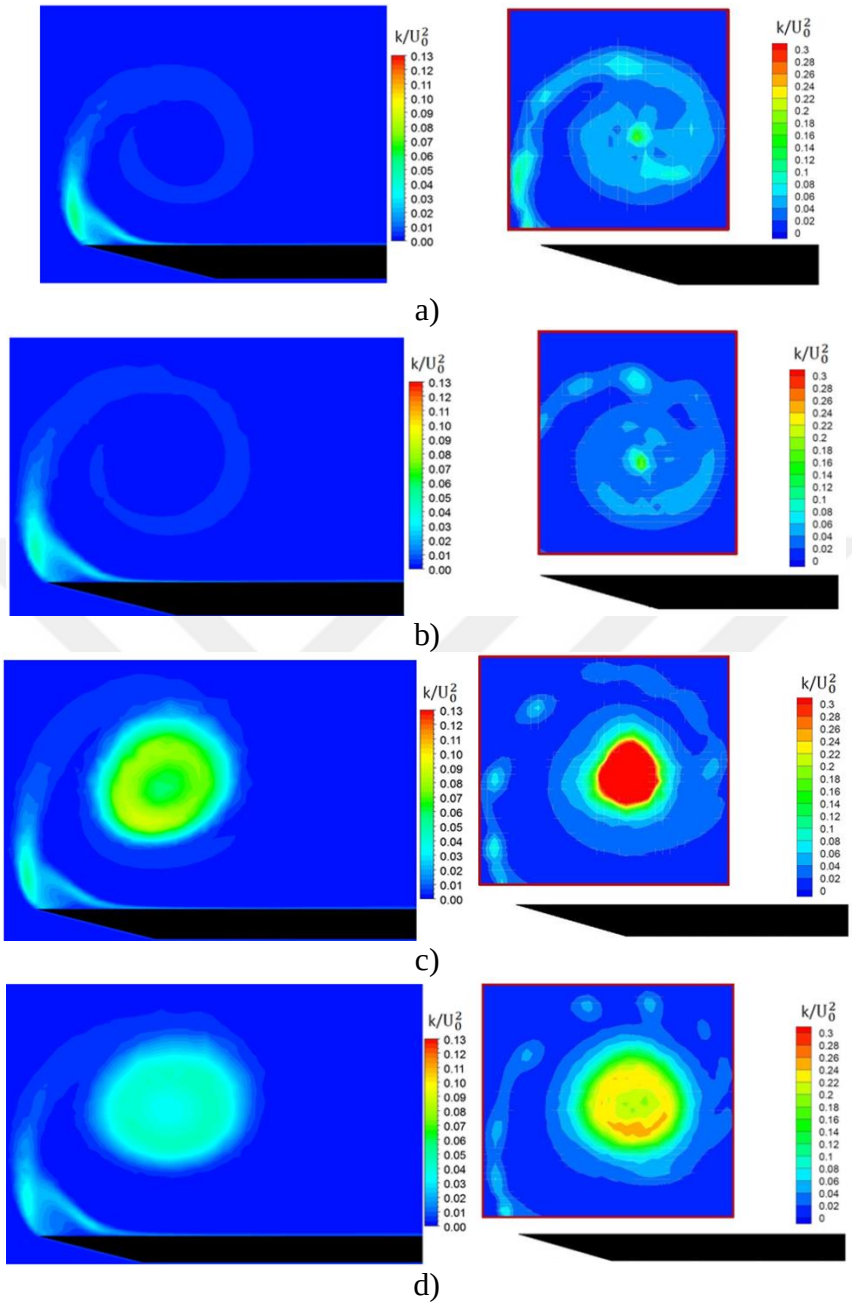

Figure 4.7 Computed (left) and measured [21] (right) non-dimensional turbulent kinetic energy ($k / (U_0)^2$) at four planes perpendicular to the leeward surface of the delta wing: a) X = 500 mm, b) X = 600 mm, c) X = 700 mm, and d) X = 800 mm

CHAPTER 5

FLOW CONTROL

In this section, the flow control strategy to delay vortex breakdown location is explained in detail.

As discussed in the previous chapter, k-ω SST CC and k-ω SST LRC CC turbulence models proposed the closest value to the time-averaged vortex breakdown location of Mitchell's study [20, 21]. Since k-ω SST CC gave slightly higher suction peak than k-ω SST LRC CC turbulence model, it is used in the flow control simulations.

According to Gursul [47], along-the-core blowing is the most effective technique amongst various blowing/suction methods, and the effectiveness of that technique can be seen in Figure 2.25. For this reason, along-the-core blowing technique is applied in order to delay vortex breakdown location by adding momentum, which is expressed by a momentum coefficient (C_μ) to the vortex core. The momentum coefficient is calculated as follows:

$$C_\mu = \frac{\dot{m}V_j}{q_0 S} \tag{5.1}$$

in which $\dot{m}$ denotes the mass flow rate of the jet, V_j is the exit velocity of jet, $q_0 = (\frac{1}{2}\rho U_0^2)$ is the dynamic pressure, and S is the wing planform area. Since simulations are performed using symmetry boundary conditions, a half wing planform area is used for the parameter S in equation 5.1.

As mentioned earlier in detail, the blowing port location closest to the wing apex (at 30 % of the root chord) was found to be the most effective position according to

Guilliot et al. [34]. Visser et al. [35] state that the effectiveness of the jet was increased as the nozzle was located closer to the apex region. In addition, the optimum position of the nozzle was reported to be closer to the leading edge by Visser et al. [35]. Therefore, the blowing port is located close to the leading edge and near the apex in this study such that the center of the blowing port is located at 15 % of the root chord, which is 142.5 mm downstream from the apex and 35.4 mm away from the wing centerline, as shown in Figure 5.1. This location is underneath the vortex core. Figure 5.2 shows the jet blowing angles (azimuthal angle and pitch angle). Azimuthal angle is measured counter-clockwise from a line parallel to the root chord of the delta wing, and pitch angle is measured from the leeward surface of the wing. Since the effects of two parameters, pitch angle and momentum coefficient, are investigated in this study, azimuthal angle is kept constant and taken as 180°. The reason behind taking the azimuthal angle as 180° is the wind tunnel test results of Guillot et al. [34] with delta wing having 60° sweep angle. According to that study, optimum azimuthal angle is not the vortex core azimuthal angle, which is 158°, but rather it is 170°. By examining the angle difference between optimum azimuthal angle and vortex core azimuthal angle in the study of Guillot et al. [34] which is approximately 12°, 180° azimuthal angle is evaluated to be a proper choice for the present study. This is because angle difference between the optimum azimuthal angle and the vortex core azimuthal angle is around 13°, which is a very close value to the study of Guillot et al. [34].

The first series of simulations (p-cases) are conducted to observe the influence of pitch angle with constant C_μ on vortex breakdown location, as shown in Table 5.1 and Figure 5.3. The dashed line in Figure 5.3 shows the vortex breakdown location of the non-controlled simulation. These simulations show that the cases with pitch angle ranging from 7.5° to 30° exhibit greater delay. After 30°, there is a quite linear relationship between pitch angle and delay such that an increase in pitch angle causes a reduction in vortex breakdown delay. It is important to recall that vortex breakdown location (X_b / c) is equal to 0.66 for the non-controlled case.

A second series of simulations (m-cases) are conducted to determine the momentum coefficient (C_μ) dependence of vortex breakdown location with constant pitch angle, as shown in Table 5.2 and Figure 5.4. The dashed line in Figure 5.4 shows the vortex breakdown location of the non-controlled simulation. It is clearly seen that as C_μ increases, the location of vortex breakdown is placed further downstream of the wing. Cases p3 and m5 have an equal C_μ and pitch angle; the only difference is the jet area, and thus jet velocity. It is seen that jet velocity has an influence on vortex breakdown location. The higher the jet velocity, the greater the delay of vortex breakdown is. In order to visualize vortex breakdown delay, the non-dimensional axial velocity contour at a plane passing through the vortex core for the non-controlled case and the m1 case is shown in Figure 5.5.

It is important to note that the number of grids used in the flow control simulations is higher than the mesh 3 case due to the mesh refinement in the blowing location. Increase in number of grids causes slightly higher computation time than Mesh 3 case as discussed in chapter 3.

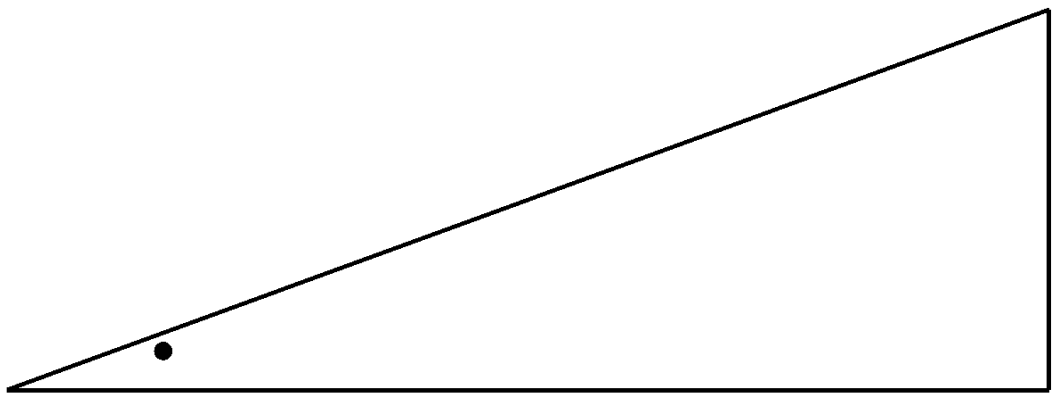

Figure 5.1 Location of the blowing port

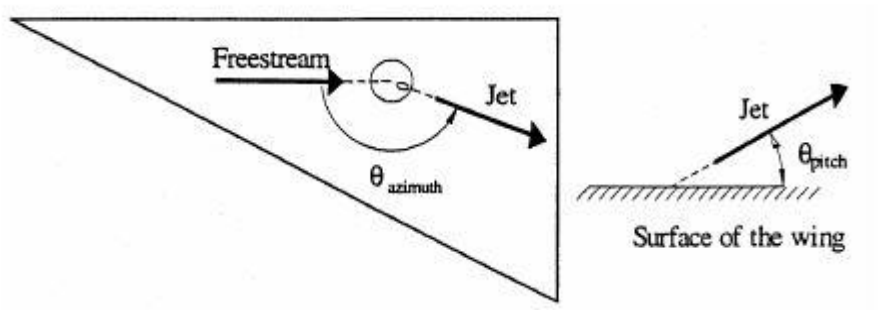

Figure 5.2 Jet blowing angle: a) Azimuthal angle, b) Pitch angle [45]

Table 5.1 First set of simulations

Case	Pitch angle (°)	Cμ	Breakdown location (Xb/c)	Jet velocity (m/s)
p1	7.5	0.008	0.72	100
p2	15	0.008	0.72	100
p3	30	0.008	0.72	100
p4	45	0.008	0.69	100
p5	60	0.008	0.67	100

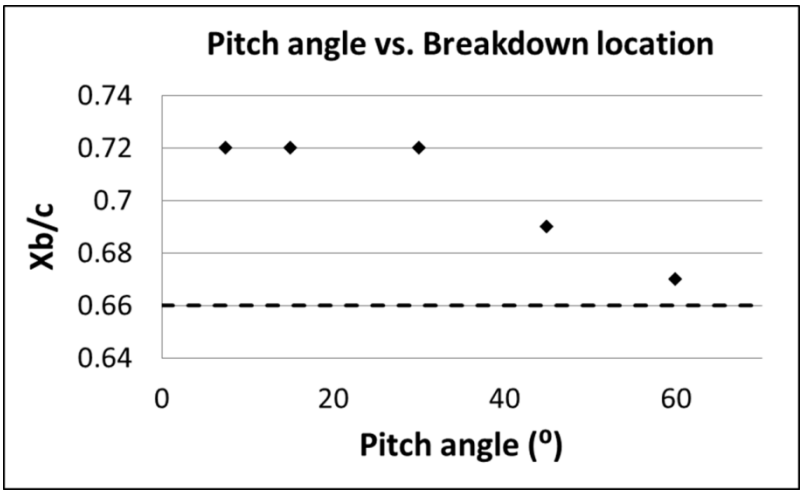

Figure 5.3 Results of the first set of simulations

Table 5.2 Second set of simulations

Case	Cμ	Breakdown location (Xb/c)	Jet velocity (m/s)	Pitch angle (°)
m1	0.048	0.84	100	30
m2	0.036	0.81	86.6	30
m3	0.024	0.79	70.71	30
m4	0.012	0.75	50	30
m5	0.008	0.71	40.82	30

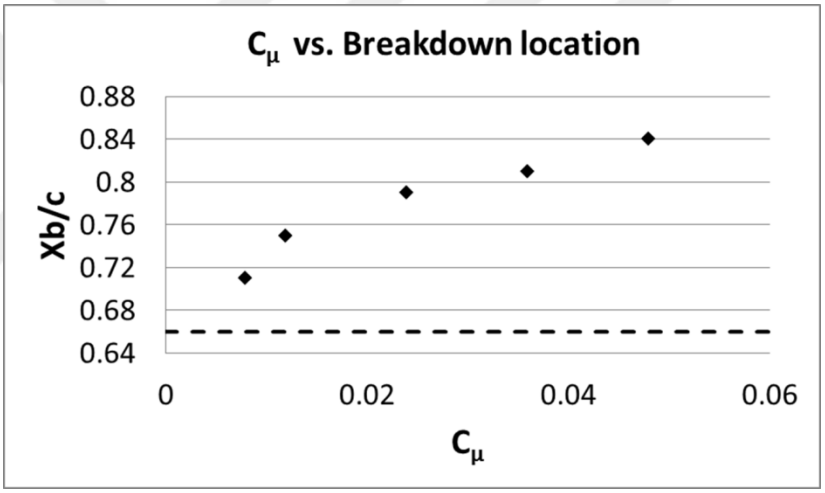

Figure 5.4 Results of the second set of simulations

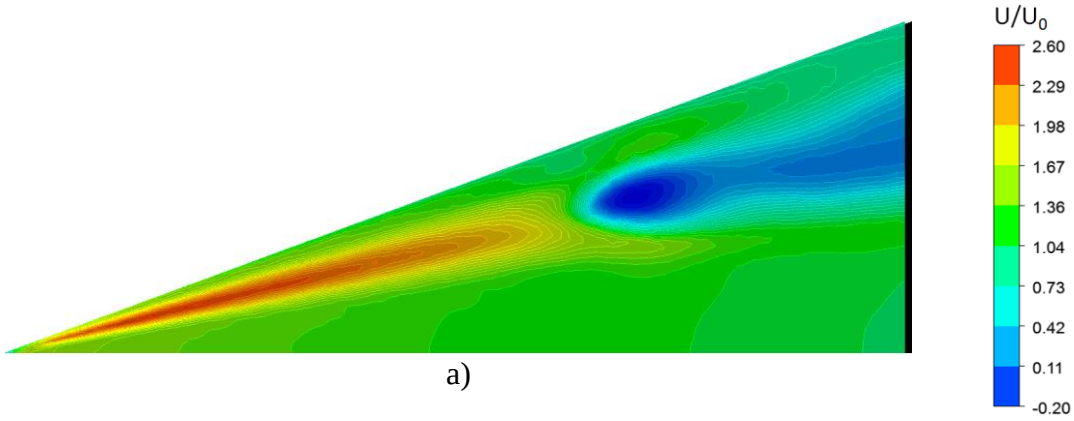

a)

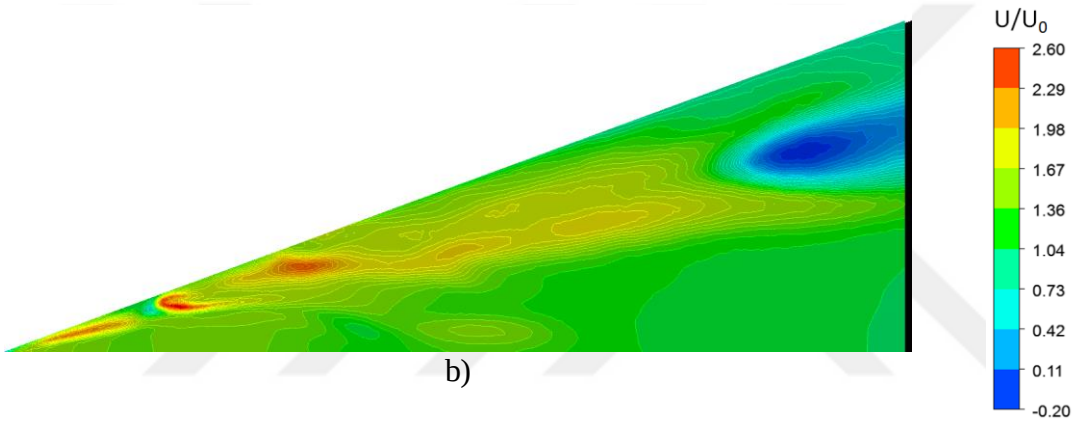

b)

Figure 5.5 Non-dimensional axial velocity contour at a plane passing through the vortex core for a) non-controlled case, and b) controlled case, m1

CHAPTER 6

CONCLUSIONS

6.1 Summary and Conclusions

The flow around the delta wing consists of several vortical structures, and leading edge vortices are the most evident of these vortical structures; they are formed by roll up of the shear layer or vortex sheet. Leading edge vortices create suction peaks on the leeward surface of the delta wing and hereby produce significant lift gain. At sufficiently high angles of attack, the cores of leading edge vortices stagnate and experience a sudden expansion and disorganization, also known as vortex breakdown. There are undesired effects of the vortex breakdown phenomenon including rapid changes in forces and moments exerted on delta wings. Therefore, predicting and controlling vortex breakdown location is important to ensure aerodynamic stability.

The flow around the delta wing having 70° sweep angle is studied in this work using a computational fluid dynamics approach. Firstly, a mesh independence study was conducted by tracking Cp and vortex breakdown location. The selected mesh consists of approximately 10 million elements and contains both tetrahedral and prismatic elements. When the selected mesh is compared with a higher mesh density case which consists of approximately 15 million elements, it is observed that the vortex breakdown location does not change and that the peak magnitude of Cp does not vary more than 2 %.

Different turbulence models and corrections including k-ω SST LRC- CC, k-ω SST LRC, k-ω SST CC, k-ω SST, Spalart-Allmaras CC, Spalart-Allmaras, and k-ω LRC- SFC- CC are compared and validated against Mitchell's study [20 ,21].

According to the vortex breakdown locations obtained from computations, k-ω SST CC and k-ω SST LRC-CC predictions are the same and equal to 66 % of the root chord which is the closest value to the time-averaged vortex breakdown location (65 %) of the Mitchell's experimental study [20,21]. According to Cp results, k-w-SST CC is higher and hence closer to experimental data than the k-w-SSR LRC-CC turbulence model. Therefore, k-ω SST CC is the turbulence model used in the flow control simulations. It is also notable that enabling the CC option moves the vortex breakdown location to upstream and provides a more accurate solution.

The current study proposes the one of the closest vortex breakdown location to the experimental result among the previously conducted numerical studies. All of the conducted studies including the current study underestimate the surface pressure coefficient (Cp). When the Cp contour of the current study is examined, it is seen that there is a qualitative agreement with the experiment. Additionally, computed Cp contour of the leeward surface captures the clue of the secondary vortex near the primary separation line (leading edge), which the Mitchel's study [21, 21] could not capture.

Quantitative agreement between the experiment [20, 21] and the current study on the suction peak location, placed at approximately 66 % of the wingspan, is observed. The angle between the vortex core and the leeward surface of the delta wing is calculated and it is concluded that the calculated angle is slightly underestimated when compared to the experimental data, which is 7°. Similarly, the calculated sweep angle of the vortex core is slightly lower than the experimental value, which is 77°.

Moreover, along-the-core blowing flow control technique is applied to delay the vortex breakdown location. The effect of two parameters, pitch angle and momentum coefficient to vortex breakdown delay are investigated in detail.

Firstly, the influence of pitch angle on delay of vortex breakdown location is investigated. It is seen that maximum vortex breakdown delay is achieved at pitch

angles from 7.5° to 30°. After 30^0, the vortex breakdown location moves upstream as the pitch angle increases. Another set of simulations are conducted to determine the effect of C_μ on vortex breakdown location. As expected, higher C_μ caused a greater delay in the vortex breakdown location. It is also a notable observation that cases having the same C_μ and the same pitch angle but different jet velocity lead to slightly different vortex breakdown delays.

6.2 Future Work

The current study has investigated the vortical flow field around the delta wing with steady state CFD models. Additional turbulence models including transition turbulence models can be investigated. Transient models can be utilized to capture the unsteady phenomena of the vortical flow field including oscillation of vortex breakdown location, vortex wandering, etc. Another important advantage of using the transient models is that the unsteady blowing which has great potential when compared with steady blowing (as shown in Figure 2.26) can be studied.

For the along-the-core flow control method, pitch angle, azimuthal angle, C_μ and location of the jet on the delta wing are the main parameters affecting the breakdown location of the vortex. In this study, pitch angle and C_μ were the only investigated parameters. The other parameters (azimuthal angle and location of the jet) were optimized by reviewing the literature due to computation time limit. In the future, effect of azimuthal angle and location of the jet to the vortex breakdown location can be investigated.

REFERENCES

1. M. Allan, “A CFD Investigation of Wind Tunnel Interference on Delta Wing Aerodynamics” Ph.D. Thesis, Department of Aerospace Engineering, University of Glasgow, 2002.

2. M. M. Yavuz, “Origin and Control of the Flow Structure and Topology on Delta Wings” Ph.D. Thesis, Department of Mechanical Engineering and Mechanics Lehigh University, U.S.A, January 2006.

3. S. Görtz, “Realistic Simulations of Delta Wing Aerodynamics Using Novel CFD Methods” Ph.D. Thesis, Department of Aeronautical and Vehicle Engineering, Royal Institute of Technology (KTH), 2005.

4. R. C. Nelson and A. Pelletier, “The Unsteady Aerodynamics of Slender Wings and Aircraft Undergoing Large Amplitude Maneuvers” Progress in Aerospace Science 39, pp. 185-248, 2003.

5. M. R. Visbal, “Computational and Physical Aspects of Vortex Breakdown on Delta Wings” 33rd Aerospace Science Meeting & Exhibit, AIAA Paper, 1995.

6. H. Werlé, “Quelques résultats expérimentaux sur les ailes en fléche, aux faibles vitesses, obtenus en tunnel hydrodynamique” La Recherche Aéronautique, no. 41, pp. 15-21, 1954.

7. N. C. Lambourne and D. W. Bryer, “The Bursting of Leading-Edge Vortices-Some Observations and Discussion of the Phenomenon”

Aeronautical Research Council Reports and Memoranda, Ministry of Aviation, no. 3282, 1962.

8. J. M. Lopez, “Axisymmetric Vortex Breakdown Part 1: Confined Swirling Flow,” Journal of Fluid Mechanics, vol. 221, pp. 533-552, 1990.

9. G. L. Brown and J. M. Lopez, “Axisymmetric Vortex Breakdown Part 2: Physical Mechanisms,” Journal of Fluid Mechanics, vol.221, pp. 553-576, 1990.

10. J. Delery, “ Aspects of Vortex Breakdown,” Progress in Aerospace Sciences, vol. 30, no. 1, pp. 1-59, 1994.

11. T. B. Benjamin, “Theory of the Vortex Breakdown Phenomenon,” Journal of Fluid Mechanics, vol. 14, no. 4, pp. 593-629, 1962.

12. M. Jones, A. Hashimoto and Y. Nakamura, “Criteria for Vortex Breakdown Above High-Sweep Delta Wings,” AIAA Journal, vol.47, no. 10, pp. 2306-2320, Oct. 2009.

13. I. Gursul, “Review of Unsteady Vortex Flows over Slender Delta Wings,” Journal of Aircraft, vol. 42, no. 2, pp. 299-319, Mar.-Apr. 2005.

14. G. S. Taylor and I. Gursul, “Buffetting Flows over a Low-Sweep Delta Wing,” AIAA Journal, vol. 42, no. 9, pp. 1737-1745, 2004.

15. A. M. Mitchell, S. Morton and J. Forsythe, “Analysis of Delta Wing Vortical Substructures Using Detached-Eddy Simulation,” AIAA Paper 2002-2968, Jun. 2002.

16. M. R. Visbal and R. E. Gordnier, “On the Structure of the Shear Layer Emanating from a Swept Leading Edge at Angle of Attack,” AIAA Paper 2003-4016, Jun. 2003.

17. I. Gursul and W. Xie, “Origin of Vortex Wandering over Delta Wings,” Journal of Aircraft, vol. 37, no. 2, pp. 348-350, 2000.

18. M. Menke and I. Gursul, “Unsteady Nature of Leading Edge Vortices,” Physics of Fluids, vol. 9, no. 10, pp. 1-7, 1997.

19. A. Mitchell, P. Molton, D. Barbaris, J. Delery, “Characterization of vortex breakdown by flow field and surface measurements,” AIAA Paper 2000-0788, Jan. 2000.

20. A. M. Mitchell, “Experimental Data Base Selected For Numerical and Analytical Validation and Verification: Onera 70-Deg Delta Wing,” NATO RTO-TR-AVT-080, chapter-3.

21. A. M. Mitchell, “Experimental Data Base Selected For NATO RTO/AVT Numerical and Analytical Validation and Verification: Onera 70-Deg Delta Wing,” AIAA Paper 2003-3941, Jun. 2003.

22. Y. Guy, J. A. Morrow and T. E. McLaughlin, “Velocity Measurements on a Delta Wing with Periodic Blowing and Suction,” AIAA Paper 200-0550, Jan. 2000.

23. J-F. Le Roy, I. Mary and O. Rodriguez, “CFD Solutions of 70° Delta Wing Flows,” AIAA Paper 2003-4219, Jun. 2003.

24. J-F. Le Roy and O. Rodriguez, “RANS Solutions of 70° Delta Wing in Steady Flow,” NATO RTO-TR-AVT-080, chapter-16.

25. S. A. Morton, J. R. Forsythe, A. M. Mitchell and D. Hajek, “DES and RANS Simulations of Delta Wing Vortical Flows,” AIAA Paper 2002-0587, Jan. 2002.

26. B. I. Soemarwoto and O. J. Boelens, “Simulation of Vortical Flow Over a Slender Delta Wing Experiencing Vortex Breakdown,” AIAA Paper 2003-4215, Jun. 2003.

27. B. I. Soemarwoto and O. J. Boelens, “Simulation of Vortical Flow Over Onera 70-Degree Delta Wing Experiencing Vortex Breakdown,” NATO RTO-TR-AVT-080, chapter-18.

28. S. Görtz, “Detached-Eddy Simulations of a Full-Span Delta Wing at High Incıdence,” AIAA Paper 2003-4216, Jun. 2003.

29. M. R. Allan, K. J. Badcock and B. E. Richards, “A CFD Investigation of Wind Tunnel Wall Influences on Pitching Delta Wings,” AIAA Paper 2002-2938, Jun. 2002.

30. Y. Le Moigne and A. Rizzi, “Grid Study for Euler Simulations of a 70° Delta Wing with the Unstructured Flow Solver Edge,” NATO RTO-TR-AVT-080, chapter-14.

31. S. Morton, “Detached-Eddy Simulations of Vortex Breakdown over a 70-Degree Delta Wing,” Journal of Aircraft, vol. 46, no. 3, pp. 746-755, May-Jun. 2009.

32. A. M. Mitchell, J. Delery, “Research into Vortex Breakdown Control,” Progress in Aerospace Sciences, vol. 37, no. 4, pp. 385-418, May 2001.

33. C-H. Kuo, N-Y. Lu, “Unsteady vortex structure over delta wing subject to transient along core blowing,” AIAA Journal, vol. 36, no. 9, pp. 1658-1664, 1998.

34. S. Guillot, E. J. Gutmark and T. J. Garrison, “Delay of vortex breakdown over a delta wing via near-core blowing,” AIAA Paper 98-0315, Jan. 1998.

35. K. D. Visser, K. P. Iwanski, R. C. Nelson and T. T. Ng, “Control of leading edge vortex breakdown by blowing,” 26th AIAA Aerospace Sciences meeting, AIAA Paper 88-0504, Jan. 1988.

36. A. M. Mitchell, D. Barberis, P. Molton and J. Delery, “Oscillation of vortex breakdown location and control of the time-averaged location by blowing,” AIAA Journal, vol. 33, no. 5,pp. 793-803, 2000.

37. A. M. Mitchell, D. Barberis, P. Molton and J. Delery, “Control of vortex breakdown location by symmetric and asymmetric blowing,” 30th AIAA Fluid Dynamics Conference AIAA Paper 99-3652, 1999.

38. A. M. Mitchell, P. Molton, D. Barberis and J-L Gobert, “Control of vortex breakdown by along-the-core blowing,” AIAA Fluids 2000 Conference, AIAA Paper 00-2608, June 2000.

39. M. Kyriakou, D. Missirlis and K. Yakinthos, “Numerical modeling of the vortex breakdown phenomenon on a delta wing with trailing-edge jet-flap,” International Journal of Heat and Fluid Flow, vol. 31, no. 6, pp. 1087-1095, December 2010.

40. C. Shih and Z. Ding, “Trailing-edge jet control of leading edge vortices of delta wing,” AIAA Journal, vol. 34 no. 7, pp. 1447-1456, 1996.

41. Z. Vlahostergios, D. Missirlis, K. Yakinthos and A. Goulas, “Computational modeling of vortex breakdown control on a delta wing,” International Journal of Heat and Fluid Flow, vol. 39, pp. 64-77, 2013.

42. J. Cai, S. Pan, W. Li and Z. Zhang, “Numerical and experimental investigations of a nonslender delta wing with leading-edge vortex flap,” Computers & Fluids, vol. 99, pp. 1-17, July 2014.

43. R. M. Cummings, S. A. Morton and S. G. Siegel, “Computational Simulation and PIV Measurements of the Laminar Vortical Flowfield for a Delta Wing at High Angle of Attack,” AIAA Paper 2003-1102, 2003.

44. J. A. Freeman, “Computational fluid dynamics investigations of vortex breakdown for a delta wing at high angle of attack,” M. S. Thesis, Air Force Institute of Technology, AFIT/GAE/ENY/03-3, 2003.

45. S. Muramatsu, S. Okada and K. Hiraoka, “Numerical analysis of control of leading-edge vortex on delta wing with blowing,” 23rd AIAA Applied Aerodynamics Conference, AIAA Paper 2005-5088, 2005.

46. H. S. Chung, C. A. Seaver and T. E. McLaughlin, “Vortex flow control over a delta wing by co-rotating and counter-rotating vortex generator,” 28th AIAA Applied Aerodynamics Conference, AIAA Paper 2010-4952, 2010.

47. I. Gursul, Z. Wang and E. Vardaki, “Review of flow control mechanisms of leading-edge vortices,” Progress in Aerospace Sciences, vol. 43, pp. 246-270, 2007.

48. Ansys Fluent Theory Guide, Release 14.5, 2012.

APPENDIX A

TURBULENCE MODELING

In this chapter, Reynolds-Averaged Navier Stokes (RANS) models are briefly explained.

A1. Reynolds Averaging and Boussinesq Approach

Parameters of the Navier Stokes equations can be decomposed into mean and fluctuating components. Velocity components can be decomposed as:

$$u_i = \overline{u_i} + u_i' \tag{A.1}$$

where $\overline{u_i}$ and u_i' are the mean and the fluctuating components of the velocity components, respectively.

Similarly, scalar quantities like pressure and energy can be expressed as follows:

$$\phi = \overline{\phi} + \phi' \tag{A.2}$$

Substituting the decomposed form of the solution variables into the instantaneous governing equations (continuity and momentum) and taking the ensemble (time) average leads to ensemble-averaged momentum equations. The Cartesian tensor forms of these equations are:

Mass conservation equation:

$$\frac{\partial \rho}{\partial t} + \frac{\partial}{\partial x_i}(\rho \overline{u_i}) = 0 \tag{A.3}$$

where t is time, ρ is density, and $\overline{u_i}$ is the time average of fluid velocity.

Momentum conservation equation:

$$\begin{aligned} \frac{\partial}{\partial t}(\rho \overline{u_i}) + \frac{\partial}{\partial x_j}\left(\rho \overline{u_i}\,\overline{u_j}\right) \\ = -\frac{\partial \overline{p}}{\partial x_i} + \frac{\partial}{\partial x_j}\left[\mu\left(\frac{\partial \overline{u_i}}{\partial x_j} + \frac{\partial \overline{u_j}}{\partial x_i} - \frac{2}{3}\delta_{ij}\frac{\partial \overline{u_k}}{\partial x_k}\right)\right] \\ + \frac{\partial}{\partial x_j}\left(-\rho \overline{u_i' u_j'}\right) \end{aligned} \tag{A.4}$$

where $\overline{p}$ designates the mean pressure, μ shows the dynamic viscosity, δ_{ij} is the Kronecker delta, and $-\rho \overline{u_i' u_j'}$ is called as the Reynolds stress tensor. Modeling of Reynolds stresses is required to close the Reynolds averaged momentum equations.

A common modeling approach is the Boussinesq approach that relates the Reynolds stresses to the mean velocity gradients:

$$-\rho \overline{u_i' u_j'} = \mu_t\left(\frac{\partial \overline{u_i}}{\partial x_j} + \frac{\partial \overline{u_j}}{\partial x_i}\right) - \frac{2}{3}\left(\rho k + \mu_t \frac{\partial \overline{u_k}}{\partial x_k}\right)\delta_{ij} \tag{A.5}$$

where μ_t denotes the turbulent viscosity. Following models use the Boussinesq hypothesis: The Spalart-Allmaras model, the k-ε models, and the k-ω models. One additional transport equation for turbulent viscosity (μ_t) is solved in the Spalart-Allmaras model. For the k-ε and k-ω turbulence models, additionally two transport equations, either for turbulence kinetic energy (k) and dissipation of turbulence (ε)

or turbulence kinetic energy (k) and specific dissipation rate (ω), are solved. Turbulent viscosity (μ_t) is calculated in terms of either turbulence kinetic energy (k) and turbulence dissipation (ε) or turbulence kinetic energy (k) and specific dissipation rate (ω) .

A2. Shear-Stress Transport (SST) k-ω Model

Menter's shear-stress transport (SST) k-ω model [48] is utilized in the simulations and evaluated to detect vortex breakdown location more precisely among other RANS turbulence models so that only the details of this model are represented. The SST k-ω model is analogous to the standard k-ω model with additional refinements. This model effectively blends the k-ω model in the near-wall region and the k-ε model in the region away from the surface with the help of a blending function. Modified turbulent viscosity is used in the SST k-ω model when involving the transport of the turbulent shear stress. A damped cross-diffusion derivative term in the ω equation is incorporated in the SST k-ω model. Further features and refinements evoke the SST k-ω model to be more accurate, with the flow having adverse pressure gradient, airfoils, and transonic shock waves in comparison with the standard k-ω model.

The transport equations for the SST k-ω model are given as:

$$\frac{\partial}{\partial t}(\rho k) + \frac{\partial}{\partial x_i}(\rho k \overline{u_i}) = \frac{\partial}{\partial x_j}\left(\Gamma_k \frac{\partial k}{\partial x_j}\right) + \tilde{G}_k - Y_k + S_k \qquad \text{(A.6)}$$

and

$$\frac{\partial}{\partial t}(\rho\omega) + \frac{\partial}{\partial x_j}\left(\rho\omega\overline{u_j}\right) = \frac{\partial}{\partial x_j}\left(\Gamma_\omega \frac{\partial \omega}{\partial x_j}\right) + G_\omega - Y_\omega + D_\omega + S_\omega \qquad \text{(A.7)}$$

where $\tilde{G}_k$ indicates the turbulence kinetic energy generation due to mean velocity gradient and G_ω represents the generation of specific dissipation rate (ω). The effective diffusivity of the k and ω are denoted as Γ_k and Γ_ω, respectively. In addition, dissipation of k and ω by reason of turbulence are represented as Y_k and Y_ω, respectively. The cross-diffusion term is represented by D_ω. S_k and S_ω are the user-defined source terms.

Effective diffusivities for k and ω are given as:

$$\Gamma_k = \mu + \frac{\mu_t}{\sigma_k} \qquad \text{(A.8)}$$

$$\Gamma_\omega = \mu + \frac{\mu_t}{\sigma_\omega} \qquad \text{(A.9)}$$

where σ_k and σ_ω denote the turbulent Prandtl numbers for production (k) and dissipation (ω). Turbulent viscosity (μ_t) is calculated as:

$$\mu_t = \frac{\rho k}{\omega} \frac{1}{max\left[\frac{1}{\alpha^*}, \frac{SF_2}{a_1\omega}\right]} \qquad \text{(A.10)}$$

where strain rate magnitude is represented as S and

$$\sigma_k = \frac{1}{F_1/\sigma_{k,1} + (1 - F_1)/\sigma_{k,2}} \qquad \text{(A.11)}$$

$$\sigma_\omega = \frac{1}{F_1/\sigma_{\omega,1} + (1 - F_1)/\sigma_{\omega,2}} \qquad \text{(A.12)}$$

where a_1, $\sigma_{k,1}$, $\sigma_{k,2}$, $\sigma_{\omega,1}$, $\sigma_{\omega,2}$ are model constants and α^* is the coefficient that damps the turbulent viscosity causing a low-Reynolds number correction. It is defined as:

$$\alpha^* = \alpha_\infty^* \left(\frac{\alpha_0^* + Re_t/R_k}{1 + Re_t/R_k} \right) \tag{A.13}$$

where R_k, α_0^*, α_∞^* are model constants and

$$Re_t = \frac{\rho k}{\mu \omega} \tag{A.14}$$

Blending functions F_1 and F_2 are given as:

$$F_1 = tanh(\phi_1^4) \tag{A.15}$$

$$\phi_1 = \min\left[max\left(\frac{\sqrt{k}}{0.09\omega y}, \frac{500\mu}{\rho y^2 \omega} \right), \frac{4\rho k}{\sigma_{\omega,2} D_\omega^+ y^2} \right] \tag{A.16}$$

$$D_\omega^+ = max\left[2\rho \frac{1}{\sigma_{\omega,2}} \frac{1}{\omega} \frac{\partial k}{\partial x_j} \frac{\partial \omega}{\partial x_j}, 10^{-10} \right] \tag{A.17}$$

$$F_2 = tanh(\phi_2^2) \tag{A.18}$$

$$\phi_2 = max\left[2\frac{\sqrt{k}}{0.09\omega y}, \frac{500\mu}{\rho y^2 \omega} \right] \tag{A.19}$$

where y represents the distance to the next surface and D_ω^+ represents the positive section of the cross-diffusion term.

As mentioned previously, the term $\tilde{G}_k$ represents the production of turbulence kinetic energy and is defined as:

$$\tilde{G}_k = \min(G_k, 10\rho\beta^* k\,\omega) \tag{A.20}$$

where β^* is a model constant and G_k is defined as:

$$G_k = -\rho\overline{u_i' u_j'}\frac{\partial \overline{u_j}}{\partial x_i} \tag{A.21}$$

The evaluation of G_k utilizing the Boussinesq hypothesis is accomplished by:

$$G_k = \mu_t S^2 \tag{A.22}$$

In the above equation, S represents the modulus of the mean rate of strain tensor and it is defined as:

$$S \equiv \sqrt{2S_{ij}S_{ij}} \tag{A.23}$$

Production of the ω represented as G_ω in the transport equations is defined as:

$$G_\omega = \frac{\alpha}{\nu_t}\tilde{G}_k \tag{A.24}$$

where

$$\nu_t = \mu_t \rho \tag{A.25}$$

and

$$\alpha = \frac{\alpha_\infty}{\alpha^*}\left(\frac{\alpha_0 + Re_t/R_\omega}{1 + Re_t/R_\omega}\right) \tag{A.26}$$

where α_0 and R_ω are model constants, α^* is previously defined in (A.13), and α_∞ is given by

$$\alpha_\infty = F_1\alpha_{\infty,1} + (1 - F_1)\alpha_{\infty,2} \tag{A.27}$$

where

$$\alpha_{\infty,1} = \frac{\beta_{i,1}}{\beta_\infty^*} - \frac{\kappa^2}{\sigma_{w,1}\sqrt{\beta_\infty^*}} \tag{A.28}$$

$$\alpha_{\infty,2} = \frac{\beta_{i,2}}{\beta_\infty^*} - \frac{\kappa^2}{\sigma_{w,2}\sqrt{\beta_\infty^*}} \tag{A.29}$$

where $\beta_{i,1}$, $\beta_{i,2}$, β_∞^* are model constants and κ is 0.41.

The term Y_k in the transport equation shows the dissipation of turbulence kinetic energy (k) and is described as:

$$Y_k = \rho\beta^* k\omega \tag{A.30}$$

where

$$\beta^* = \beta_i^*[1 + \zeta^* F(M_t)] \tag{A.31}$$

$$\beta_i^* = \beta_\infty^*\left(\frac{4/15 + (Re_t/R_\beta)^4}{1 + (Re_t/R_\beta)^4}\right) \tag{A.32}$$

where ζ^* , R_β, β_∞^* are model constants, Re_t is given in equation (A.14), and $F(M_t)$ denotes the compressibility function:

$$F(M_t) = \begin{cases} 0 & M_t < M_{t0} \\ M_t^2 - M_{t0}^2 & M_t > M_{t0} \end{cases} \tag{A.33}$$

where

$$M_t^2 \equiv \frac{2k}{a^2} \tag{A.34}$$

$$a = \sqrt{\gamma RT} \tag{A.35}$$

where γ, R, T and M_{t0} denote the ratio of specific heats, the gas-law constant, the temperature and the model constant, respectively.

Y_ω term in the transport equations shows the dissipation of ω and is desribed as:

$$Y_\omega = \rho\beta\omega^2 \tag{A.36}$$

where

$$\beta = \beta_i\left[1 - \frac{\beta_i^*}{\beta_i}\zeta^* F(M_t)\right] \tag{A.37}$$

where β_i^* and $F(M_t)$ are given in (A.32) and (A.33), respectively. ζ^* is model constant and β_i is given as:

$$\beta_i = F_1\beta_{i,1} + (1 - F_1)\beta_{i,2} \tag{A.38}$$

where $\beta_{i,1}$ and $\beta_{i,2}$ are model constants and F_1 is a blending function obtained from (A.15).

Transformation of the standard k-ε model into the equations based on k and ω in order to blend the k-ε and k-ω models leads to the introduction of a cross-diffusion term (D_ω) that is given by

$$D_\omega = 2(1 - F_1)\rho\frac{1}{\omega\sigma_{\omega,2}}\frac{\partial k}{\partial x_j}\frac{\partial \omega}{\partial x_j} \tag{A.39}$$

Eddy viscosity models are insensitive to streamline curvature and system rotation, which have a considerable impact on many turbulent flows. In order to sensitize the standard eddy viscosity models to the effects of streamline curvature and system rotation, a modification to the turbulence production term is available in ANSYS Fluent. Modification of the production term is used as a multiplier of the production term [48].